

OEDG: OSCILLATION-ELIMINATING DISCONTINUOUS GALERKIN METHOD FOR HYPERBOLIC CONSERVATION LAWS *

MANTING PENG[†], ZHENG SUN[‡], AND KAILIANG WU[§]

Abstract. Controlling spurious oscillations is crucial for designing reliable numerical schemes for hyperbolic conservation laws. This paper proposes a novel, robust, and efficient oscillation-eliminating discontinuous Galerkin (OEDG) method on general meshes, motivated by the damping technique in [Lu, Liu, and Shu, *SIAM J. Numer. Anal.*, 59:1299–1324, 2021]. The OEDG method incorporates an OE procedure after each Runge–Kutta stage, and it is devised by alternately evolving the conventional semidiscrete DG scheme and a damping equation. A novel damping operator is carefully designed to possess both *scale-invariant* and *evolution-invariant* properties. We rigorously prove *optimal error estimates* of the *fully discrete* OEDG method for smooth solutions of linear scalar conservation laws. This might be the first generic fully-discrete error estimates for *nonlinear* DG schemes with an automatic oscillation control mechanism. The OEDG method exhibits many notable advantages. It effectively eliminates spurious oscillations for challenging problems spanning various scales and wave speeds, all without necessitating problem-specific parameters. It also obviates the need for characteristic decomposition in hyperbolic systems. Furthermore, it retains the key properties of the conventional DG method, such as conservation, optimal convergence rates, and superconvergence. Moreover, the OEDG method maintains stability under the normal CFL condition, even in the presence of strong shocks associated with highly stiff damping terms. The OE procedure is *non-intrusive*, facilitating seamless integration into existing DG codes as an independent module. Its implementation is straightforward and efficient, involving only simple multiplications of modal coefficients by scalars. The OEDG approach provides new insights into the damping mechanism for oscillation control. It reveals the role of the damping operator as a modal filter and establishes close relations between the damping technique and spectral viscosity techniques. Extensive numerical results confirm the theoretical analysis and validate the effectiveness and advantages of the OEDG method.

Key words. Hyperbolic conservation laws, discontinuous Galerkin method, oscillation control, damping technique, scale-invariant, optimal error estimates

MSC codes. 65M60, 65M12, 35L65

1. Introduction. Discontinuous Galerkin (DG) methods, originally introduced by Reed and Hill [28] in 1973, are a class of finite element methods employing discontinuous piecewise polynomial spaces. Since the series of pioneering work by Cockburn and Shu [9, 8, 7, 6, 10], the DG methods coupled with Runge–Kutta (RK) time discretization have become a prominent approach for solving hyperbolic conservation laws of the form

$$(1.1) \quad \mathbf{u}_t + \nabla \cdot \mathbf{f}(\mathbf{u}) = \mathbf{0},$$

with applications in diverse fields including computational fluid dynamics. In this paper, we further develop the DG methods and focus on a novel numerical approach to control spurious oscillations near discontinuities, such as shocks.

The solution of nonlinear hyperbolic conservation laws may develop discontinuities within finite time, even starting from smooth initial conditions. This poses significant challenges in numerical simulations, as many schemes may generate spurious oscillations near these discontinuities. Such oscillations can give rise to nonphysical wave structures, numerical instability, or even result in blow-up solutions. Consequently, controlling spurious oscillations is paramount in the design of robust numerical schemes for hyperbolic conservation laws. For DG methods, two primary strategies exist to mitigate oscillations. The first strategy is to apply suitable limiters, such as the total variation diminishing limiter, total variation bounded limiter, and weighted essentially nonoscillatory type limiters; see, for example, [29, 27, 41]. These limiters serve to adjust the slopes or point values of the solution in some troubled cells, acting as postprocessors for the DG solution after each time

*M. Peng and K. Wu was partially supported by Shenzhen Science and Technology Program (No. RCJC20221008092757098) and National Natural Science Foundation of China (No. 12171227). Z. Sun was partially supported by NSF grant DMS-2208391.

[†]Department of Mathematics, Southern University of Science and Technology, Shenzhen, Guangdong 518055, China.

[‡]Department of Mathematics, The University of Alabama, Tuscaloosa, AL 35487, USA (zsun30@ua.edu).

[§]Corresponding author. Department of Mathematics and SUSTech International Center for Mathematics, Southern University of Science and Technology, and National Center for Applied Mathematics Shenzhen (NCAMS), Shenzhen, Guangdong 518055, China (wukl@sustech.edu.cn).

step or RK stage. While effective, limiters may be problem-dependent and can potentially alter some desirable properties of the original DG scheme. Another strategy is to incorporate appropriate artificial viscosity terms with second or higher order spatial derivatives to diffuse off the oscillations. We refer to [43, 17, 38, 18] and the references therein for related works.

In recent works [24, 21], Lu, Liu, and Shu systematically developed the so-called oscillation-free DG (OFDG) method, which innovatively incorporates damping terms to suppress spurious oscillations. The semidiscrete OFDG method can be expressed as an ordinary differential equation (ODE) system:

$$(1.2) \quad \frac{d\mathbf{U}}{dt} + \mathbf{L}_f(\mathbf{U}) + \mathbf{\Sigma}(\mathbf{U})\mathbf{U} = \mathbf{0},$$

where \mathbf{U} denotes the DG modal coefficients, $\mathbf{L}_f(\mathbf{U})$ corresponds to the conventional DG spatial discretization of $\nabla \cdot \mathbf{f}(\mathbf{u})$, and $\mathbf{\Sigma}(\mathbf{U})\mathbf{U}$ represents the added damping terms penalizing the deviation between the DG solution and its low-order polynomial projections. The OFDG method shares a similar flavor with local projection stabilization schemes [2, 3]. A notable feature of the OFDG scheme is the inclusion of predefined damping coefficients $\mathbf{\Sigma}(\mathbf{U})$, which allows for its applicability to a wide range of common problems. In theory, Lu, Liu, and Shu [24] rigorously established the stability, optimal error estimates, and superconvergence of the OFDG method for scalar conservation laws. The extension to systems of hyperbolic conservation laws was further studied in [21], and applications to other equations were explored in [22, 34, 13]. However, for discontinuous problems, the damping terms render the ODE system (1.2) highly stiff and lead to very restricted time step sizes for explicit schemes, as mentioned in [21]. To mitigate this challenge, the (modified) exponential RK methods [20] are typically required [21].

This paper proposes and analyzes a new efficient DG approach, termed oscillation-eliminating DG (OEDG) method, designed on general meshes. While our focus is on hyperbolic conservation laws, the OEDG method is applicable to general time-dependent partial differential equations (PDEs) with discontinuous solutions. The OEDG approach is inspired by the OFDG method [24, 21], incorporating a similar oscillation control strategy but from a different novel perspective, which results in significant enhancements in implementation and robustness. The new innovations, contributions, and findings in this work are detailed in the following subsections.

1.1. Algorithmic innovations and contributions. The OEDG method is designed by alternately evolving the conventional semidiscrete DG scheme for (1.1) and a quasi-linear damping ODE:

$$(1.3) \quad \frac{d\mathbf{U}}{dt} = -\mathbf{L}_f(\mathbf{U}) \quad \text{and} \quad \frac{d\mathbf{U}_\sigma}{dt} = -\tilde{\mathbf{\Sigma}}(\mathbf{U})\mathbf{U}_\sigma.$$

The damping equation is devised for eliminating spurious oscillations. Here $\tilde{\mathbf{\Sigma}}(\mathbf{U})$ is a new damping operator, which differs from $\mathbf{\Sigma}(\mathbf{U})$, and is carefully constructed to achieve the scale-invariant and evolution-invariant properties. With orthogonal DG basis functions, $\tilde{\mathbf{\Sigma}}(\mathbf{U})$ simplifies to a diagonal matrix. Notably, once $\tilde{\mathbf{\Sigma}}(\mathbf{U})$ is fixed, the quasi-linear damping ODE in (1.3) can be *solved exactly* using a simple exponential operator. This splitting strategy is integrated into the RK stages or multi-steps. For example, with a second-order RK method, the fully discrete OEDG scheme is represented as

$$(1.4) \quad \begin{aligned} \mathbf{U}^* &= \mathbf{U}_\sigma^n - \tau \mathbf{L}_f(\mathbf{U}_\sigma^n), & \mathbf{U}_\sigma^* &= e^{-\tau \tilde{\mathbf{\Sigma}}(\mathbf{U}^*)} \mathbf{U}^*, \\ \mathbf{U}^{n+1} &= \frac{1}{2}(\mathbf{U}_\sigma^n + \mathbf{U}_\sigma^*) - \frac{\tau}{2} \mathbf{L}_f(\mathbf{U}_\sigma^*), & \mathbf{U}_\sigma^{n+1} &= e^{-\tau \tilde{\mathbf{\Sigma}}(\mathbf{U}^{n+1})} \mathbf{U}^{n+1}. \end{aligned}$$

Note that although the OEDG method employs a seemingly “first-order” splitting (1.3) in the time evolution, this does *not* affect the order of accuracy, since the damping term $-\tilde{\mathbf{\Sigma}}(\mathbf{U})\mathbf{U}_\sigma$ is a high-order term for smooth solutions. Indeed, the optimal convergence rates of the OEDG method can be rigorously proven in theory; see Section 4.

The OEDG method offers many notable advantages. First, it effectively eliminates the spurious oscillations *for problems across different scales and wave speeds, without relying on problem-specific parameters*. It also retains many desirable properties of the original DG method, including *conservation*,

high-order accuracy, optimal fully-discrete error estimates in theory, and numerical *superconvergence* for linear scalar conservation laws. Moreover, thanks to the exact solver for the damping equation in (1.3) with the new coefficients $\tilde{\Sigma}(\mathbf{U})$, the OEDG method exhibits some distinctive features not found in the OFDG method:

- *Non-intrusive*: The OE procedure is fully detached from the RK stage update and does not interfere with the DG spatial discretization. Hence it can be incorporated non-intrusively into existing DG codes as an independent module. This makes the OEDG approach applicable to general time-dependent PDEs with discontinuous solutions. Note that such a non-intrusive feature is not possessed by the (modified) exponential RK method employed in the OFDG method [21].
- *Simple and efficient*: Implementing the OE procedure is straightforward and efficient on general meshes, as it only involves the multiplication of modal coefficients by scalars.
- *Stable with normal time step sizes*: Thanks to the exact solver for the OE step, the OEDG method remains stable under the normal CFL condition, even in the presence of strong shocks associated with highly stiff damping terms. Unlike the OFDG method, there is no need to use the (modified) exponential RK methods to avoid stringent time step restrictions.
- *Scale-invariant and evolution-invariant*: The OEDG method adopts the new damping operator $\tilde{\Sigma}(\mathbf{U})$, which is carefully designed such that the damping effect remains scale-invariant and evolution-invariant. These key properties are crucial for guaranteeing the oscillation-free property, enabling the OEDG method to perform consistently well for problems across various scales and wave speeds. It is observed that the damping operator $\Sigma(\mathbf{U})$ employed in the OFDG method, as described in [24, Equation (2.12)], lacks information about wave speed and scales linearly with respect to the solution magnitude: $\Sigma(\lambda\mathbf{U}) = |\lambda|\Sigma(\mathbf{U})$. While this damping operator performs well for many common problems, it may exhibit excessive smearing or persistent spurious oscillations for ultra-fast/ultra-slow flows or solutions with large/small magnitudes; see Figure 1.
- *Free of characteristic decomposition*: The OEDG method does not require characteristic decomposition for hyperbolic systems, as the OE procedure applied directly to the conservative variables typically deliver satisfactory results. This feature simplifies the implementation and reduces the computational costs. It also distinguishes the OEDG method from the OFDG method with non-scale-invariant damping, in which characteristic decomposition can be necessary for some challenging problems (as seen in [21, Figure 3.5] and Figure 4 in the present paper). Note that, without scale-invariant damping coefficients, it can be difficult to select the appropriate scale of eigenvectors in the characteristic decomposition, because eigenvectors are nonunique and can be scaled by a nonzero scalar. Different scaled eigenvectors will result in different characteristic variables, which lead to different damping strengths. Consequently, if the scheme lacks scale invariance, its numerical performance heavily relies on the choice of eigenvectors, as improper selections can result in excessive smearing or persistent spurious oscillations.

All these features highlight the differences between the OEDG and OFDG methods. The last two features can be attributed to our novel damping operator. It is worth noting that this new operator, if integrated into the OFDG method in place of its original damping operator, may also offer these two features.

1.2. New insights and findings. By decoupling the OE step from the RK stage update, the OEDG method provides new insights into understanding the damping mechanism for oscillation control. Based on the exact solver for the damping equation in (1.3), we discover that the damping operator acts as a modal filter, revealing close relations between the oscillation-free damping technique and the spectral viscosity techniques [14, 16, 15]. This perspective may not be obviously observed in the OFDG method [24, 21]. In addition, the exact solver for the damping equation leads to insights into designing the scale-invariant and evolution-invariant damping operator. As shown in (1.4), the coefficients $\tau\tilde{\Sigma}(\mathbf{U})$ as arguments of an exponential must be dimensionless. The scale-invariant property $\tilde{\Sigma}(\lambda\mathbf{U} + \mu) = \tilde{\Sigma}(\mathbf{U})$ for any nonzero λ and the inclusion of wave speed in the damping coefficients are crucial to ensure that $\tau\tilde{\Sigma}(\mathbf{U})$ is dimensionless.

1.3. Theoretical contributions and innovations. We carry out a comprehensive fully-discrete error analysis of the proposed OEDG methods of arbitrarily high order accuracy in space and time.

We rigorously establish the optimal error estimates of the fully-discrete OEDG methods for the linear advection equation with smooth solutions on Cartesian meshes. It is worth noting that, despite the linearity of the model equation considered in the analysis, the OE procedure transforms the DG scheme into a nonlinear one. Consequently, the error analysis is quite nontrivial and presents technical challenges akin to those encountered in fully discrete error estimates for nonlinear hyperbolic equations. A key innovation in our analysis lies in ingeniously transforming the nonlinear OEDG formulation into a linear RKDG method augmented by a nonlinear source term. This transformation allows us to leverage the techniques developed in [36, 35, 1] for the original RKDG methods. One of the major difficulties in our analysis pertains to estimating the perturbation of the numerical solution during the OE step based on appropriate a priori assumptions, which is then integrated into the fully-discrete error analysis of the OEDG method. These estimates introduce essential complexities not encountered in the semidiscrete error analysis of the OFDG method [24]. To the best of our knowledge, the presented optimal error analysis might be the first generic fully-discrete error estimates of nonlinear DG schemes with an automatic oscillation control mechanism for conservation laws.

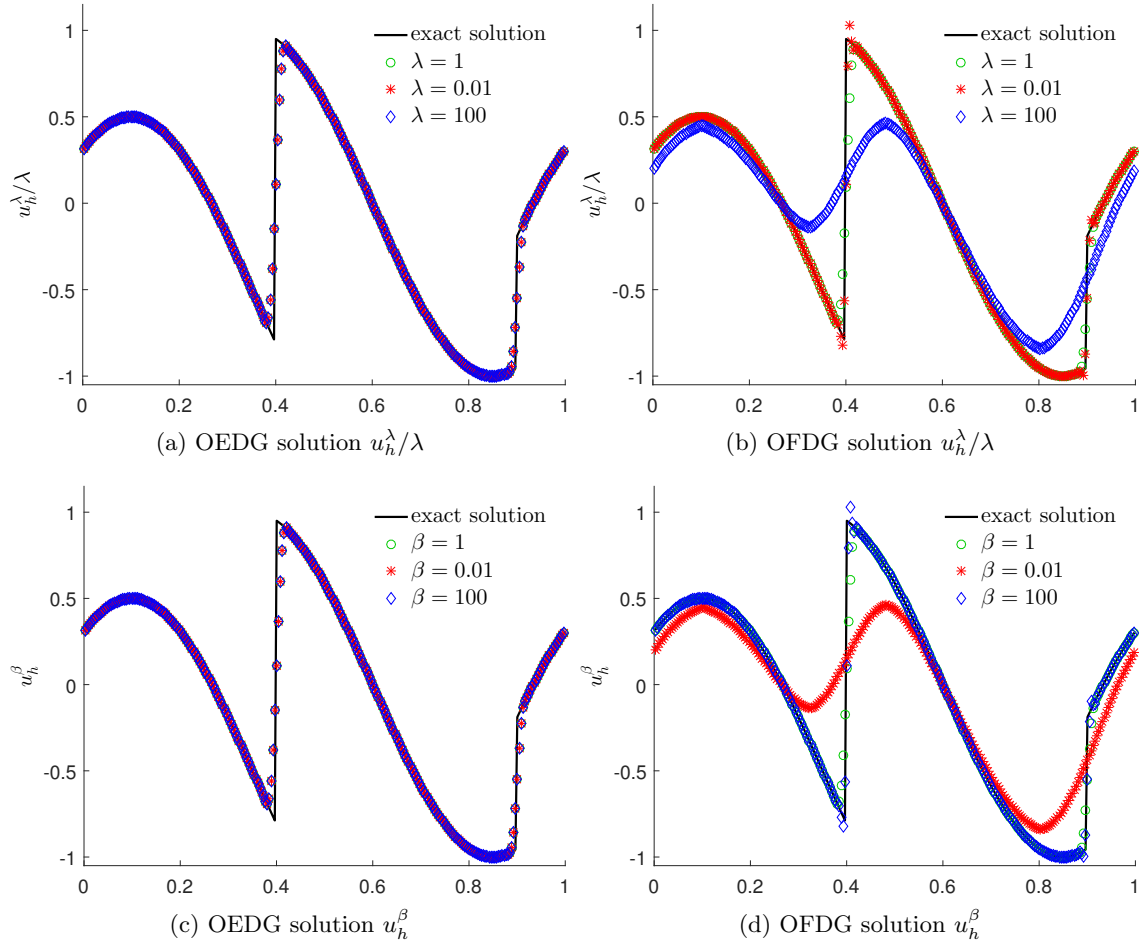


Fig. 1: Comparisons of third-order OEDG and OFDG methods for problems of different scales and wave speeds. The cell averages of the DG solutions are plotted: u_h^λ denotes numerical solutions at $t = 1.1$ for $u_t + u_x = 0$ with scaled initial data $u(x, 0) = \lambda u_0(x)$; u_h^β denotes numerical solutions at $t = 1.1/\beta$ for $u_t + \beta u_x = 0$ with $u(x, 0) = u_0(x)$, where $u_0(x)$ is defined in (5.1). See Example 5.2 for the detailed setup. The OFDG method exhibits excessive smearing or persistent spurious oscillations (overshoots or undershoots) in large or small scale cases, while OEDG method performs consistently well thanks to scale invariance and evolution invariance. The results of OFDG method can be improved if our new scale-invariant and evolution-invariant damping is used instead.

This paper is structured as follows: Section 2 introduces the OEDG method for one-dimensional hyperbolic conservation laws, with extensions to multiple dimensions discussed in Section 3. Optimal error estimates of the fully discrete OEDG method for linear advection equation are established in Section 4. Section 5 provides extensive numerical examples to verify the effectiveness and advantages of the OEDG method, before conclusions in Section 6.

2. OEDG method for one-dimensional conservation laws. This section presents the OEDG scheme for 1D hyperbolic conservation laws

$$(2.1) \quad u_t + f(u)_x = 0.$$

We first assume (2.1) is a scalar conservation law, and will discuss the extension to hyperbolic systems later in Subsection 2.4.

2.1. Formulation of OEDG method. Let $\Omega = \cup_j I_j$ with $I_j = [x_{j-\frac{1}{2}}, x_{j+\frac{1}{2}}]$ be a partition of the 1D spatial domain Ω . Denote $h_j = x_{j+\frac{1}{2}} - x_{j-\frac{1}{2}}$. The DG finite element space is defined as follows:

$$\mathbb{V}^k := \{v \in L^2(\Omega) : v|_{I_j} \in \mathbb{P}^k(I_j) \forall j\},$$

where $\mathbb{P}^k(I_j)$ is the space of polynomials of degree less than or equal to k on I_j .

Let us first review the conventional DG method. The conventional semidiscrete DG method seeks the numerical solutions $u_h(\cdot, t) \in \mathbb{V}^k$ such that for any test functions $v \in \mathbb{V}^k$,

$$(2.2) \quad \int_{I_j} (u_h)_t v dx = \int_{I_j} f(u_h) v_x dx - \hat{f}_{j+\frac{1}{2}} v_{j+\frac{1}{2}}^- + \hat{f}_{j-\frac{1}{2}} v_{j-\frac{1}{2}}^+,$$

where $v_{j+\frac{1}{2}}^\pm := \lim_{\epsilon \rightarrow 0^+} v(x_{j+\frac{1}{2}} \pm \epsilon)$, and $\hat{f}_{j+\frac{1}{2}}$ is a suitable numerical flux, for example, a monotone flux in the scalar case. The semidiscrete scheme (2.2) can be rewritten in an ODE form $\frac{d}{dt} u_h = L_f(u_h)$, which can be further discretized in time with some high-order accurate RK or multi-step methods. For example, the DG method coupled with an r th-order s -stage RK method reads

$$\begin{aligned} u_h^{n,0} &= u_h^n, \\ u_h^{n,\ell+1} &= \sum_{0 \leq m \leq \ell} (c_{\ell m} u_h^{n,m} + \tau d_{\ell m} L_f(u_h^{n,m})), \quad \ell = 0, 1, \dots, s-1, \\ u_h^{n+1} &= u_h^{n,s}, \end{aligned}$$

where u_h^n is the numerical solution at n th time level, τ is the time step-size, and $\sum_{0 \leq m \leq \ell} c_{\ell m} = 1$.

Define $u_\sigma^0 = u_h^0$. Now we present the OEDG method with an OE procedure applied after each RK stage:

$$(2.3) \quad u_h^{n,\ell+1} = \sum_{0 \leq m \leq \ell} (c_{\ell m} u_\sigma^{n,m} + \tau d_{\ell m} L_f(u_\sigma^{n,m})),$$

$$(2.4) \quad u_\sigma^{n,\ell+1} = \mathcal{F}_\tau u_h^{n,\ell+1}, \quad \ell = 0, 1, \dots, s-1.$$

For ease of notation, we define $u_\sigma^{n,0} = u_\sigma^n$ and $u_\sigma^{n+1} = u_\sigma^{n,s}$. Here (2.4) is the OE procedure, with $\mathcal{F}_\tau : \mathbb{V}^k \rightarrow \mathbb{V}^k$ being the solution operator of a damping equation. More specifically, we define $(\mathcal{F}_\tau u_h^{n,\ell+1})(x) = u_\sigma(x, \tau)$ with $u_\sigma(x, \hat{t}) \in \mathbb{V}^k$ being the solution to the following initial value problem:

$$(2.5) \quad \begin{cases} \frac{d}{d\hat{t}} \int_{I_j} u_\sigma v dx + \sum_{m=0}^k \beta_j \frac{\sigma_j^m (u_h^{n,\ell+1})}{h_j} \int_{I_j} (u_\sigma - P^{m-1} u_\sigma) v dx = 0 \quad \forall v \in \mathbb{P}^k(I_j), \\ u_\sigma(x, 0) = u_h^{n,\ell+1}(x), \end{cases}$$

where \hat{t} is a pseudo-time different from t , and β_j is a suitable estimate of the local maximum wave speed on I_j ; for scalar conservation laws, we take $\beta_j = |f'(\bar{u}_j^{n,\ell+1})|$, where $\bar{u}_j^{n,\ell+1}$ denotes the cell

average of $u_h^{n,\ell+1}(x)$ over I_j . The operator P^m is the standard L^2 projection into \mathbb{V}^m for $m \geq 0$, that is, for any function w , $P^m w \in \mathbb{V}^m$ satisfies

$$\int_{I_j} (P^m w - w) v dx = 0 \quad \forall v \in \mathbb{P}^m(I_j), \forall j.$$

We define $P^{-1} = P^0$. It is worth noting that $P^0 w(x) = \bar{w}_j$ for all $x \in I_j$, where \bar{w}_j denotes the cell average of w over I_j . The damping coefficient $\sigma_j^m(u_h)$, as a function of u_h , is crucial and should be chosen carefully. It should be small in smooth regions and large near discontinuities. To make the resulting scheme scale-invariant, we propose a new damping coefficient

$$(2.6) \quad \sigma_j^m(u_h) = \begin{cases} 0, & \text{if } u_h \equiv \text{avg}(u_h), \\ (2m+1)h_j^m \frac{|\llbracket \partial_x^m u_h \rrbracket_{j-\frac{1}{2}} \rrbracket + |\llbracket \partial_x^m u_h \rrbracket_{j+\frac{1}{2}} \rrbracket}{(2k-1)m! \cdot 2\|u_h - \text{avg}(u_h)\|_{L^\infty(\Omega)}}, & \text{otherwise,} \end{cases}$$

where $\llbracket v \rrbracket_{j+\frac{1}{2}} = v_{j+\frac{1}{2}}^+ - v_{j+\frac{1}{2}}^-$ is the jump of v at $x = x_{j+\frac{1}{2}}$, and $\text{avg}(v) = \frac{1}{|\Omega|} \int_{\Omega} v(x) dx$ denotes the average of v over Ω . Note that the common scalar quantity $\|u_h - \text{avg}(u_h)\|_{L^\infty(\Omega)}$ is used for all mesh cells. At the beginning of the OE procedure in each stage, this quantity can be first calculated using global data, similarly to how we compute τ at every time step. After that, the computation of $\sigma_j^m(u_h)$ will involve information only from I_j and its adjacent cells, which maintains the compactness and local structure of the conventional DG methods. As it will be elaborated in Subsection 2.3, the OEDG method is scale-invariant and evolution-invariant, thanks to the carefully designed new damping coefficient (2.6) and the incorporation of wave speed β_j into the damping terms in (2.5).

2.2. Exact solver of OE procedure. Note that $\sigma_j^m(u_h^{n,\ell+1})$ in (2.5) only depends on the ‘‘initial’’ solution $u_\sigma(x, 0) = u_h^{n,\ell+1}(x)$. As a result, the damping ODE (2.5) is linear, and its exact solution can be *explicitly* formulated. Therefore, the OE procedure is computationally cheap and very easy to implement.

Let $\{\phi_j^{(i)}(x)\}_{i=1}^k$ be a local orthogonal basis of $\mathbb{P}^k(I_j)$ over I_j . For example, we choose the scaled Legendre polynomials

$$\phi_j^{(0)}(x) = 1, \quad \phi_j^{(1)}(x) = \frac{x - x_j}{h_j}, \quad \phi_j^{(2)}(x) = 12 \left(\frac{x - x_j}{h_j} \right)^2 - 1, \quad \dots$$

Assume that the solution of (2.5) can be represented as

$$(2.7) \quad u_\sigma(x, \hat{t}) = \sum_{i=0}^k u_j^{(i)}(\hat{t}) \phi_j^{(i)}(x) \quad \text{for } x \in I_j.$$

Note that

$$(2.8) \quad (u_\sigma - P^{m-1} u_\sigma)(x, \hat{t}) = \sum_{i=\max\{m,1\}}^k u_j^{(i)}(\hat{t}) \phi_j^{(i)}(x).$$

Substitute (2.7)–(2.8) into (2.5) and take $v = \phi_j^{(i)}$. For $i \geq 1$, one obtains

$$\frac{d}{d\hat{t}} u_j^{(i)}(\hat{t}) \int_{I_j} \left(\phi_j^{(i)}(x) \right)^2 dx + \sum_{m=0}^i \beta_j \frac{\sigma_j^m}{h_j} u_j^{(i)}(\hat{t}) \int_{I_j} \left(\phi_j^{(i)}(x) \right)^2 dx = 0, \quad i = 1, 2, \dots, k,$$

which can be simplified as

$$(2.9) \quad \frac{d}{d\hat{t}} u_j^{(i)}(\hat{t}) + \left(\frac{\beta_j}{h_j} \sum_{m=0}^i \sigma_j^m \right) u_j^{(i)}(\hat{t}) = 0, \quad i = 1, 2, \dots, k.$$

Solving (2.9) gives

$$(2.10) \quad u_j^{(i)}(\tau) = \exp\left(-\frac{\beta_j \tau}{h_j} \sum_{m=0}^i \sigma_j^m\right) u_j^{(i)}(0), \quad i = 1, 2, \dots, k.$$

For $i = 0$, since $\int_{I_j} (u_\sigma - P^{m-1} u_\sigma) \phi_j^{(0)} dx \equiv 0$, we have $\frac{d}{dt} u_j^{(0)}(t) \int_{I_j} (\phi_j^{(0)}(x))^2 dx = 0$ and thus

$$(2.11) \quad u_j^{(0)}(\tau) = u_j^{(0)}(0).$$

Hence, with (2.11) and (2.10), one has

$$(2.12) \quad u_\sigma^{n,\ell+1} = \mathcal{F}_\tau u_h^{n,\ell+1} = u_\sigma(x, \tau) = u_j^{(0)}(0) \phi_j^{(0)}(x) + \sum_{i=1}^k e^{-\frac{\beta_j \tau}{h_j} \sum_{m=0}^i \sigma_j^m} \sigma_j^m(u_h^{n,\ell+1}) u_j^{(i)}(0) \phi_j^{(i)}(x),$$

where $u_j^{(i)}(0) = \int_{I_j} u_h^{n,\ell+1} \phi_j^{(i)} dx / \|\phi_j^{(i)}\|_{L^2(I_j)}^2$ is the modal coefficient of $u_h^{n,\ell+1}(x)$.

Remark 2.1 (dimensionless damping). As well-known, the argument of an exponential must be dimensionless, since it is raised to all powers in the corresponding series expansion and maintaining consistent dimensions across all terms in the series is imperative. For the exponential term in (2.12), the scale-invariant property in Theorem 2.6 ensures that $\sigma_j^m(u_h^{n,\ell+1})$ is inherently dimensionless, while the inclusion of the wave speed β_j in the damping terms guarantees that $\frac{\beta_j \tau}{h_j}$ is also dimensionless.

Remark 2.2 (conservation). From (2.11), one can see that the OE procedure does not affect the modal coefficient associated with $\phi_j^{(0)}$. In other words, the OE procedure does not alter the cell average of the numerical solution, thereby preserving the local mass conservation.

Remark 2.3 (stability). From (2.12), one can observe that the damping operator actually acts as a modal filter. This reveals the close relations between the damping technique and the spectral viscosity techniques [14, 16, 15]. The OE procedure damps the modal coefficients of the high-order moments of the numerical solution. Hence we have

$$\|u_\sigma^{n,\ell+1}\|_{L^2(I_j)}^2 = \sum_{i=0}^k |u_j^{(i)}(\tau)| \|\phi_j^{(i)}\|_{L^2(I_j)}^2 \leq \sum_{i=0}^k |u_j^{(i)}(0)| \|\phi_j^{(i)}\|_{L^2(I_j)}^2 = \|u_h^{n,\ell+1}\|_{L^2(I_j)}^2.$$

As a result, the OE procedure will reduce the element-wise L^2 norm of the numerical solution, thereby enhancing the stability of the numerical solution. Thanks to the exact solver for the OE step, the OEDG method remains stable under the normal CFL condition, even in the presence of strong shocks associated with highly stiff damping terms. Unlike the OFDG approach [21], the OEDG method does not require the (modified) exponential RK methods to avoid stringent time step restrictions.

Remark 2.4 (simplicity and efficiency). The OE procedure is fully detached from the RK stage update and does not interfere with the DG spatial discretization. In contrast to the exponential RK method in the OFDG approach, the OE procedure in the OEDG method is non-intrusive: It can be incorporated easily and seamlessly into existing DG codes as an independent module, requiring only a slight modification to the existing structure, rather than an extensive overhaul. Moreover, implementing the OE procedure is straightforward and efficient, as it involves only simple multiplication of modal coefficients by scalars.

Remark 2.5. In the OE procedure (2.4), it seems unnecessary to synchronize the time stepsize with the specific RK stage. We opt to evolve the damping equation over a full time step for ease, which also promotes uniformity in the implementation of the OE procedure. Certainly, one can choose to align the time stepsize with the specific RK stage, which may help reduce the damping strength.

2.3. Scale invariance and evolution invariance. In this subsection, we elaborate the scale-invariant and evolution-invariant properties of the OEDG method, which are attained through the carefully designed new damping operator.

THEOREM 2.6 (scale invariance). *For any $\lambda \neq 0$ and any $\mu \in \mathbb{R}$, ones has*

$$\sigma_j^m(\lambda u_h + \mu) = \sigma_j^m(u_h),$$

which implies

$$\mathcal{F}_\tau(\lambda u_h + \mu) = \lambda \mathcal{F}_\tau(u_h) + \mu.$$

Such a scale-invariant property is crucial, as it ensures that the damping coefficient (2.6) is “dimensionless” and that the damping strength/effect remains unchanged regardless of the unit used for u . For instance, if u represents mass, then the scale-invariant damping effect is consistent, whether gram or kilogram is used for u . Additionally, we observe that scale invariance is vital for effectively guaranteeing the oscillation-free property, enabling the OEDG method to perform consistently well for problems across different scales; see Figure 1 and more numerical evidences in Section 5.

Let \mathcal{S}_t be the exact solution operator of the equation (2.1), i.e., $\mathcal{S}_t(u(x, 0)) = u(x, t)$. Let \mathcal{E}_n be the solution operator of the OEDG method, i.e., $\mathcal{E}_n(u_h^0) = u_h^n$. When the flux in (2.1) is homogeneous, namely, $f(\lambda u) = \lambda f(u)$ for all λ , then the exact solution operator \mathcal{S}_t is also homogeneous: $\mathcal{S}_t(\lambda u(x, 0)) = \lambda \mathcal{S}_t(u(x, 0))$. Thanks to the scale-invariant property, the OEDG solution operator preserves such homogeneity.

THEOREM 2.7 (homogeneity). *If the flux function $f(u)$ and the numerical flux $\hat{f}_{j+\frac{1}{2}}$ are both homogeneous, then the OEDG solution operator is homogeneous:*

$$\mathcal{E}_n(\lambda u_h^0) = \lambda \mathcal{E}_n(u_h^0) \quad \forall \lambda \in \mathbb{R}.$$

Proof. If $f(u)$ and $\hat{f}_{j+\frac{1}{2}}$ are homogeneous, then $L_f(u_\sigma^{n,m})$ is homogeneous, implying that the local solution operator for each RK stage (2.3) is homogeneous. According to Theorem 2.6, the operator $\mathcal{F}_\tau(u_h)$ for each OE procedure (2.4) is homogeneous. Therefore, \mathcal{E}_n is homogeneous. \square

Remark 2.8. The following damping coefficient was proposed in [24]:

$$(2.13) \quad \hat{\sigma}_j^m(u_h) = \frac{2(2m+1)h^m}{(2k-1)m!} \left(\left[\partial_x^m u_h \right]_{j-\frac{1}{2}}^2 + \left[\partial_x^m u_h \right]_{j+\frac{1}{2}}^2 \right)^{\frac{1}{2}} \quad \text{with } h := \max_j h_j,$$

which is not scale-invariant due to $\hat{\sigma}_j^m(\lambda u_h) = |\lambda| \hat{\sigma}_j^m(u_h)$. This indicates that if we scale u by changing its unit, then the damping effect would be reduced ($|\lambda| < 1$) or increased ($|\lambda| > 1$). As a result, oscillations may not be fully suppressed for small-scale problems, and much smearing or dissipation is produced for large-scale problems; see Figure 1b, Example 5.2, and Example 5.4.

Remark 2.9 (local scale invariance). When simulating some multi-scale problems that simultaneously involve both small and large magnitude structures, one may consider a locally scale-invariant damping coefficient, for example,

$$(2.14) \quad \tilde{\sigma}_j^m(u_h) = \begin{cases} 0, & \text{if } u_h|_{\Omega_j} \equiv \text{constant}, \\ C_{m,k} \frac{(2m+1)h_j^m \tilde{h}_j}{(2k-1)m!} \frac{\left| \left[\partial_x^m u_h \right]_{j-\frac{1}{2}} \right| + \left| \left[\partial_x^m u_h \right]_{j+\frac{1}{2}} \right|}{2 \left\| u_h - \frac{1}{|\Omega_j|} \int_{\Omega_j} u_h dx \right\|_{L^\infty(\Omega_j)}}, & \text{otherwise,} \end{cases}$$

where Ω_j is a local region containing I_j and can be defined as $\Omega_j = I_{j-1} \cup I_j \cup I_{j+1}$, and $\tilde{h}_j := \max\{h_{j-1}, h_j, h_{j+1}\}$ is introduced to ensure accuracy. Yet, our numerical experiments indicate that it is difficult to determine a unified mesh-independent constant $C_{m,k}$. This will be explored in our future work. The importance of local scale invariance was also recognized in the design of finite volume and finite difference schemes [4, 12].

Another distinctive feature in the OEDG method is that our damping terms in (2.5) incorporate the information of the local maximum wave speed β_j , which was not considered in [24] but is critical for ensuring the appropriate damping strength for varying characteristic speeds (see Figure 1 and

Example 5.2). The insights of including β_j arise from the evolution-invariant property, as explained in the following. For any given constant $\lambda > 0$, let \mathcal{S}_t^λ be the solution operator of the scalar conservation law $u_t + \lambda f(u)_x = 0$. In particular, \mathcal{S}_t denotes the solution operator of equation (2.1). The equation $u_t + \lambda f(u)_x = 0$ can be regarded as the formulation of equation (2.1) by changing the unit of t . Obviously, we have the following evolution-invariant property

$$\mathcal{S}_t^\lambda = \mathcal{S}_{\lambda t} \quad \forall \lambda > 0, \quad \forall t > 0.$$

This property is also preserved by the OEDG method, as shown below. It states that for problems with slow-propagating waves (large time steps) and fast-propagating waves (small time steps), if their solutions are consistent, the OEDG method will yield identical results after a fixed number of steps.

THEOREM 2.10 (evolution invariance). *Let \mathcal{E}_n^λ be the solution operator of the OEDG method solving $u_t + \lambda f(u)_x = 0$ for $\lambda > 0$ on a fixed mesh with the same CFL number, namely, $\mathcal{E}_n^\lambda(u_h^0) = u_h^n$ at time $t_n^\lambda = n\tau_\lambda$, where $\tau_\lambda = \tau/\lambda$ is the time stepsize. Then we have*

$$(2.15) \quad \mathcal{E}_n^\lambda = \mathcal{E}_n \quad \forall \lambda > 0,$$

where \mathcal{E}_n is the solution operator of the OEDG method solving equation (2.1).

Proof. Note that the evolution-invariant property holds for the conventional DG scheme at each RK stage, because $L_{\lambda f}(u_h) = \lambda L_f(u_h)$ and $\tau_\lambda L_{\lambda f}(u_h) = \tau/\lambda \cdot \lambda L_f(u_h) = \tau L_f(u_h)$. Thus the RK stage (2.3) will be identical regardless of the value of λ . The OE step also preserves the evolution invariance. In fact, let $\mathcal{F}_{\tau_\lambda}^\lambda$ be the OE operator for $u_t + \lambda f(u)_x = 0$. Since $\beta_j = \lambda |f'(\bar{u}_j^{n,\ell+1})|$, we observe that

$$(2.16) \quad \mathcal{F}_{\tau_\lambda}^\lambda = \mathcal{F}_{\lambda\tau_\lambda} = \mathcal{F}_\tau \quad \forall \lambda > 0.$$

Consequently, both the RK stage and the OE step produce identical outputs regardless of the value of λ . Hence the OEDG method preserves the evolution invariance (2.15). \square

Remark 2.11. We would like to emphasize that the proposed damping terms offer a viable replacement for the original damping terms in the OFDG method [24, 21]. With this modification, the new OFDG method will achieve both scale invariance and evolution invariance. Consequently, it would demonstrate consistent performance across different scales and wave speeds.

2.4. Extension to 1D hyperbolic systems. The OE procedure can be naturally extended to 1D hyperbolic systems of conservation laws $\mathbf{u}_t + \mathbf{f}(\mathbf{u})_x = \mathbf{0}$. More specifically, we propose

$$(2.17) \quad \begin{cases} \frac{d}{dt} \int_{I_j} \mathbf{u}_\sigma \cdot \mathbf{v} dx + \sum_{m=0}^k \beta_j \frac{\sigma_j^m(\mathbf{u}_h^{n,\ell+1})}{h_j} \int_{I_j} (\mathbf{u}_\sigma - P^{m-1} \mathbf{u}_\sigma) \cdot \mathbf{v} dx = 0 \quad \forall \mathbf{v} \in [\mathbb{P}^k(I_j)]^N, \\ \mathbf{u}_\sigma(x, 0) = \mathbf{u}_h^{n,\ell+1}(x), \end{cases}$$

with β_j being the spectral radius of the Jacobian matrix $\frac{\partial \mathbf{f}}{\partial \mathbf{u}}(\bar{\mathbf{u}}_j^{n,\ell+1})$. The damping coefficient $\sigma_j^m(\mathbf{u}_h)$, as a function of \mathbf{u}_h , is defined as

$$\sigma_j^m(\mathbf{u}_h) := \max_{1 \leq i \leq N} \sigma_j^m(u_h^{(i)}),$$

where $u_h^{(i)}$ is the i th component of \mathbf{u}_h , and $\sigma_j^m(u_h^{(i)})$ is computed by (2.6). It can be verified that the scale-invariant and evolution-invariant properties are also satisfied by the OEDG method for hyperbolic systems.

Remark 2.12. In contrast to the OFDG method [21], characteristic decomposition appears unnecessary in the OEDG approach for hyperbolic systems. Although employing characteristic variables can aid in shock identification, determining suitable eigenvectors for the damping terms poses challenges, especially when the damping coefficients are not scale-invariant. It is crucial to note that eigenvectors

are not unique; multiplying an eigenvector by a nonzero scalar yields another valid eigenvector. Consequently, distinct (scaled) eigenvectors correspond to different characteristic variables, resulting in significantly different damping strength. Hence the numerical performance may heavily hinge on the choice of eigenvectors: Improper choices could lead to excessive smearing or persistent spurious oscillations. Moreover, opting for characteristic decomposition may destroy the scale invariance, introduce complexity in implementation, and increase computational costs.

3. OEDG method for multidimensional conservation laws. In this section, we present the OEDG method for multidimensional system of conservation laws:

$$(3.1) \quad \mathbf{u}_t + \nabla \cdot \mathbf{f}(\mathbf{u}) = \mathbf{0},$$

where $\mathbf{u} = (u_1, \dots, u_N)$. Let \mathcal{T}_h be a partition of the computational domain Ω . Our OEDG method seeks the approximate solution in the following finite element space of discontinuous functions:

$$(3.2) \quad \mathbb{V}^k := \{ \mathbf{v} \in L^2(\Omega) : \mathbf{v}|_K \in [\mathbb{P}^k(K)]^N \quad \forall K \in \mathcal{T}_h \},$$

where $\mathbb{P}^k(K)$ is the space of polynomials of total degree less than or equal to k on the element K .

The conventional semidiscrete DG method reads

$$(3.3) \quad \int_K (\mathbf{u}_h)_t \cdot \mathbf{v} d\mathbf{x} = \int_K \mathbf{f}(\mathbf{u}_h) : \nabla \mathbf{v} d\mathbf{x} - \sum_{e \in \partial K} \int_e \widehat{\mathbf{f}}(\mathbf{u}_h) : (\mathbf{n}_e \otimes \mathbf{v}) dS \quad \forall \mathbf{v} \in \mathbb{V}^k,$$

where “:” denotes the Frobenius inner product of two matrices, “ \otimes ” represents the Kronecker product of two vectors, $\widehat{\mathbf{f}}(\mathbf{u}_h)$ denotes a suitable numerical flux on the element interface $e \in \partial K$, and \mathbf{n}_e is the outward unit normal vector at e with respect to K . The semidiscrete scheme (3.3) can be rewritten in an ODE form $\frac{d}{dt} \mathbf{u}_h = L_f(\mathbf{u}_h)$, which can be further discretized in time by using some high-order accurate RK or multi-step methods.

Similar to the 1D case, the OEDG method is based on applying an OE procedure after each stage in the RK methods or each step in the multi-step methods. For example, the OEDG coupled with an r th-order s -stage RK method reads

$$(3.4) \quad \mathbf{u}_\sigma^{n,0} = \mathbf{u}_\sigma^n,$$

$$(3.5) \quad \mathbf{u}_h^{n,\ell+1} = \sum_{0 \leq m \leq \ell} (c_{\ell m} \mathbf{u}_\sigma^{n,m} + \tau d_{\ell m} L_f(\mathbf{u}_\sigma^{n,m})),$$

$$(3.6) \quad \mathbf{u}_\sigma^{n,\ell+1} = \mathcal{F}_\tau \mathbf{u}_h^{n,\ell+1}, \quad \ell = 0, 1, \dots, s-1.$$

$$(3.7) \quad \mathbf{u}_\sigma^{n+1} = \mathbf{u}_\sigma^{n,s}.$$

The OE operator \mathcal{F}_τ is defined as $(\mathcal{F}_\tau \mathbf{u}_h^{n,\ell+1})(x) = \mathbf{u}_\sigma(x, \tau)$ with $\mathbf{u}_\sigma(x, \hat{t}) \in \mathbb{V}^k$ being the solution to the following initial value problem:

$$(3.8) \quad \begin{cases} \frac{d}{d\hat{t}} \int_K \mathbf{u}_\sigma \cdot \mathbf{v} d\mathbf{x} + \sum_{m=0}^k \delta_K^m(\mathbf{u}_h^{n,\ell+1}) \int_K (\mathbf{u}_\sigma - P^{m-1} \mathbf{u}_\sigma) \cdot \mathbf{v} d\mathbf{x} = 0 \quad \forall \mathbf{v} \in [\mathbb{P}^k(K)]^N, \\ \mathbf{u}_\sigma(x, 0) = \mathbf{u}_h^{n,\ell+1}(x), \end{cases}$$

where \hat{t} is a pseudo-time different from t , P^m is the standard L^2 projection operator into \mathbb{V}^m for $m \geq 0$, and we define $P^{-1} = P^0$. The coefficient $\delta_K^m(\mathbf{u}_h)$ is defined as

$$(3.9) \quad \delta_K^m(\mathbf{u}_h) = \sum_{e \in \partial K} \beta_e \frac{\sigma_{e,K}^m(\mathbf{u}_h)}{h_{e,K}},$$

where β_e a suitable estimate of the local maximum wave speed in the direction \mathbf{n}_e on the element interface e . In our computations, we take β_e as the spectral radius of $\sum_{i=1}^d n_e^{(i)} \frac{\partial \mathbf{f}_i}{\partial \mathbf{u}} \Big|_{\mathbf{u}=\bar{\mathbf{u}}_K}$, where $n_e^{(i)}$ is the i th component of \mathbf{n}_e . We define

$$h_{e,K} = \sup_{\mathbf{x} \in K} \text{dist}(\mathbf{x}, e), \quad \sigma_{e,K}^m(\mathbf{u}_h) = \max_{1 \leq i \leq N} \sigma_{e,K}^m(u_h^{(i)})$$

with $u_h^{(i)}$ being the i th component of \mathbf{u}_h , and

$$(3.10) \quad \sigma_{e,K}^m(u_h^{(i)}) = \begin{cases} 0, & \text{if } u_h^{(i)} \equiv \text{avg}(u_h^{(i)}), \\ \frac{(2m+1)h_{e,K}^m}{2(2k-1)m!} \sum_{|\alpha|=m} \frac{\frac{1}{|e|} \int_e \|\partial^\alpha u_h^{(i)}\|_e |dS|}{\|u_h^{(i)} - \text{avg}(u_h^{(i)})\|_{L^\infty(\Omega)}}, & \text{otherwise.} \end{cases}$$

In (3.10), $|e|$ denotes the length/area of the edge/surface $e \in \partial K$, the vector $\alpha = (\alpha_1, \dots, \alpha_d)$ is the multi-index with $|\alpha| = \sum_{i=1}^d \alpha_i$, and $\partial^\alpha u_h^{(i)}$ is defined as

$$\partial^\alpha u_h^{(i)}(\mathbf{x}) = \frac{\partial^{|\alpha|}}{\partial x_1^{\alpha_1} \dots \partial x_d^{\alpha_d}} u_h^{(i)}(\mathbf{x})$$

with $\mathbf{x} = (x_1, \dots, x_d)$. In (3.10), $\|\partial^\alpha u_h^{(i)}\|_e$ denotes the absolute value of the jump of $\partial^\alpha u_h^{(i)}$ across the element interface e , and its integration on e should be approximated by some quadrature rules. In our computations for 2D problems, the trapezoidal rule is used. Similar to the 1D case, the multidimensional OE procedure can be easily implemented as

$$(3.11) \quad \mathcal{F}_\tau \mathbf{u}_h^{n,\ell+1} = \mathbf{u}_K^{(0)}(0) \phi_K^{(0)}(\mathbf{x}) + \sum_{j=1}^k e^{-\tau \sum_{m=0}^j \delta_K^m(\mathbf{u}_h^{n,\ell+1})} \sum_{|\alpha|=j} \mathbf{u}_K^{(\alpha)}(0) \phi_K^{(\alpha)}(\mathbf{x}),$$

where $\mathbf{u}_K^{(\alpha)}(0) = \int_K \mathbf{u}_h^{n,\ell+1} \phi_K^{(\alpha)} d\mathbf{x} / \|\phi_K^{(\alpha)}\|_{L^2(K)}^2$ is the expansion coefficient of $\mathbf{u}_h^{n,\ell+1}(\mathbf{x})$, and $\{\phi_K^{(\alpha)}\}_{|\alpha| \leq k}$ is a local orthogonal basis of $\mathbb{P}^k(K)$.

For example, consider a rectangular element $K = [x_{i-\frac{1}{2}}, x_{i+\frac{1}{2}}] \times [y_{j-\frac{1}{2}}, y_{j+\frac{1}{2}}]$. Define $h_{x,i} = x_{i+\frac{1}{2}} - x_{i-\frac{1}{2}}$ and $h_{y,j} = y_{j+\frac{1}{2}} - y_{j-\frac{1}{2}}$. Let β_{ij}^x and β_{ij}^y be the estimates of the local maximum wave speeds in the x - and y -directions, respectively. Then the coefficient $\delta_K^m(\mathbf{u}_h)$ becomes

$$(3.12) \quad \delta_K^m(\mathbf{u}_h) = \max_{1 \leq q \leq N} \left(\frac{\beta_{ij}^x (\sigma_{i+\frac{1}{2},j}^m(u_h^{(q)}) + \sigma_{i-\frac{1}{2},j}^m(u_h^{(q)}))}{h_{x,i}} + \frac{\beta_{ij}^y (\sigma_{i,j+\frac{1}{2}}^m(u_h^{(q)}) + \sigma_{i,j-\frac{1}{2}}^m(u_h^{(q)}))}{h_{y,j}} \right)$$

with

$$\sigma_{i+\frac{1}{2},j}^m(u_h^{(q)}) = \begin{cases} 0, & \text{if } u_h^{(q)} \equiv \text{avg}(u_h^{(q)}), \\ \frac{(2m+1)h_{x,i}^m}{2(2k-1)m!} \sum_{|\alpha|=m} \frac{\frac{1}{|h_{y,ij}|} \int_{y_{j-\frac{1}{2}}}^{y_{j+\frac{1}{2}}} \|\partial^\alpha u_h^{(q)}\|_{i+\frac{1}{2},j} |dy|}{\|u_h^{(q)} - \text{avg}(u_h^{(q)})\|_{L^\infty(\Omega)}}, & \text{otherwise,} \end{cases}$$

$$\sigma_{i,j+\frac{1}{2}}^m(u_h^{(q)}) = \begin{cases} 0, & \text{if } u_h^{(q)} \equiv \text{avg}(u_h^{(q)}), \\ \frac{(2m+1)h_{y,j}^m}{2(2k-1)m!} \sum_{|\alpha|=m} \frac{\frac{1}{|h_{x,ij}|} \int_{x_{i-\frac{1}{2}}}^{x_{i+\frac{1}{2}}} \|\partial^\alpha u_h^{(q)}\|_{i,j+\frac{1}{2}} |dx|}{\|u_h^{(q)} - \text{avg}(u_h^{(q)})\|_{L^\infty(\Omega)}}, & \text{otherwise.} \end{cases}$$

Remark 3.1. It is worth noting that the aforementioned multidimensional OE procedure maintains consistency with its 1D counterpart. Consequently, the multidimensional OEDG method, when applied on rectangular meshes for quasi-1D problems, exactly reduces to the 1D OEDG method in Section 2. Moreover, as the 1D case, the multidimensional OEDG method also satisfies the scale-invariant and evolution-invariant properties.

4. Optimal error estimates for linear advection equations. In this section, we derive error estimates of the OEDG method for the linear advection equation with constant coefficients in both 1D and 2D. To facilitate the analysis, we introduce the following nonhomogeneous equation

$$(4.1) \quad u_t + \beta \cdot \nabla u = g(\mathbf{x}, t), \quad \text{with periodic b.c.,}$$

while the error estimate will be carried out for the homogeneous case with $g \equiv 0$. Here β is a constant (vector). We assume that $\beta > 0$ in 1D and $\beta = (\beta^x, \beta^y)$ with $\beta^x > 0$ and $\beta^y > 0$ in 2D. Other cases can be proven along similar lines.

We will denote by C , possibly with subscripts, a general constant which may depend on the order of the RK method r , the number of RK stages s , the RK coefficients $c_{\ell m}$ and $d_{\ell m}$, the DG polynomial degree k , the mesh regularity constant, the Sobolev norms of the exact solution, and the final time T , etc., but is independent of the time step size τ and the mesh size h . Here h is the maximum diameter among all mesh cells. Without a subscript, C along can take different values at different places.

4.1. Main results.

THEOREM 4.1. *Consider the OEDG method with upwind flux on 1D meshes and 2D Cartesian meshes with explicit RK time stepping. Assume that the mesh partition is quasi-uniform, $\|u_h^{n,\ell} - \text{avg}(u_h^{n,\ell})\|_{L^\infty(\Omega)} \geq C > 0$ is uniformly positive for all n and ℓ , and $k > \frac{d}{2}$ and $r > \frac{d}{2} + 1$ where d is the spatial dimension. Suppose that without the OE procedure, the fully discrete RKDG scheme is stable in the sense of Assumption 4.5. If $u(x, t)$ is sufficiently smooth, and $\|u_\sigma^0 - u(\cdot, 0)\| \leq Ch^{k+1}$, then the OEDG method for (4.1) with $g \equiv 0$ (outlined in (4.12) and (4.13)) admits the optimal error estimate*

$$(4.2) \quad \max_{0 \leq n \leq n_*} \|u_\sigma^n - u(\cdot, n\tau)\| \leq C (h^{k+1} + \tau^r).$$

Here n_* is the final time step such that $T = n_*\tau$.

The proof of Theorem 4.1 will be given in Subsection 4.3.

Remark 4.2. To avoid additional technicalities and heavy notations, we assume that u is sufficiently smooth and disregard the dependence of C on the Sobolev norms of u . If it becomes necessary to optimally characterize such dependence, a set of more sophisticated reference functions must be introduced in the analysis. We refer to Remark 4.7 for further details.

Remark 4.3. By similar arguments, the error estimate can also be extended to upwind-biased flux on 1D meshes using the generalized Gauss–Radau projection [26, 5] and on special simplex meshes in two and three dimensions with the projection in [33, Lemma 3.4].

Remark 4.4. The requirement $k > \frac{d}{2}$ and $r > \frac{d}{2} + 1$ is a technical assumption specifically used in Lemma 4.10 for our proof to go through. Numerically, we still observe optimal convergence in multidimensions with low-order polynomials and RK schemes. This requirement will be used to validate the a priori (or inductive) assumption (4.20). In the error estimates of nonlinear DG schemes for time-dependent problems, it is a standard technique to first introduce an a priori assumption as in (4.20) and then validate it in the end. This technique is known to cause additional restrictions on k and r in multidimensions, unless introducing more sophisticated arguments. We refer to [39, Lemma 4.2] and [19, Lemma 3.2] for discussions on similar issues.

4.2. Notations and preliminaries. In the case that $\mathcal{F}_\tau \equiv \mathcal{I}$ is the identity operator, the OEDG scheme retrieves the RKDG scheme. Hence, it is not surprising that the error estimate of the OEDG scheme will be built upon that of the original RKDG scheme [36, 35]. This process requires the following ingredients: a special spatial projection with certain approximation and superconvergence properties, the stability of the RKDG scheme, and reference functions to track the error at each RK stage. To avoid repetitive arguments, we will introduce unified notations for both 1D and 2D cases and prove both error estimates together.

4.2.1. Projections and unified notations.

1D projection. For the 1D problem, we adopt the notations in Section 2, and denote by $(w, v) = \sum_j (w, v)_{I_j} = \sum_j \int_{I_j} w v dx$. We introduce the bilinear form for the DG operator

$$(4.3) \quad \mathcal{H}(w, v) = \beta(w, v_x) + \beta \sum_j w_{j+\frac{1}{2}}^- \llbracket v \rrbracket_{j+\frac{1}{2}}.$$

The following Gauss–Radau projection P^* will be used in the error estimates. Given w , we define P^* such that for $\eta = w - P^*w$, we have

$$(4.4) \quad (\eta, v)_{I_j} = 0 \quad \forall v \in \mathbb{P}^{k-1}(I_j) \quad \text{and} \quad P^*\eta_{j+\frac{1}{2}}^- = 0.$$

The projection has the following approximation and superconvergence properties

$$(4.5) \quad \|\eta\|_{H^m(I_j)} \leq Ch^{k+1-m}|w|_{H^{k+1}(I_j)} \quad \forall 0 \leq m \leq k+1,$$

$$(4.6) \quad \mathcal{H}(\eta, v) = 0 \quad \forall v \in \mathbb{V}^k.$$

2D projection. For the 2D problem on Cartesian meshes, we adopt the notations in Section 3. We denote by $(w, v) = \sum_{i,j} (w, v)_{K_{i,j}} = \sum_{i,j} \iint_{K_{i,j}} wv dx dy$ and introduce the bilinear form

$$(4.7) \quad \begin{aligned} \mathcal{H}(w, v) = & (w, \beta^x v_x + \beta^y v_y) - \sum_{i,j} \int_{x_{i-\frac{1}{2}}}^{x_{i+\frac{1}{2}}} \beta^y w(x, y_{j+\frac{1}{2}}^-) \left(v(x, y_{j+\frac{1}{2}}^-) - v(x, y_{j+\frac{1}{2}}^+) \right) dx \\ & - \sum_{i,j} \int_{y_{j-\frac{1}{2}}}^{y_{j+\frac{1}{2}}} \beta^x w(x_{i+\frac{1}{2}}^-, y) \left(v(x_{i+\frac{1}{2}}^-, y) - v(x_{i+\frac{1}{2}}^+, y) \right) dy. \end{aligned}$$

The following special projection from [23] will be used for optimal error estimates. Given w , we define P^* such that for $\eta = w - P^*w$, we have

$$(4.8) \quad (\eta, 1)_{K_{i,j}} = 0,$$

$$(4.9) \quad \begin{aligned} & (\eta, \beta^x v_x + \beta^y v_y)_{K_{i,j}} - \int_{x_{i-\frac{1}{2}}}^{x_{i+\frac{1}{2}}} \beta^y \eta(x, y_{j+\frac{1}{2}}^-) \left(v(x, y_{j+\frac{1}{2}}^-) - v(x, y_{j+\frac{1}{2}}^+) \right) dx \\ & - \int_{y_{j-\frac{1}{2}}}^{y_{j+\frac{1}{2}}} \beta^x \eta(x_{i+\frac{1}{2}}^-, y) \left(v(x_{i+\frac{1}{2}}^-, y) - v(x_{i+\frac{1}{2}}^+, y) \right) dy = 0 \quad \forall v \in \mathbb{P}^k(K_{i,j}). \end{aligned}$$

The projection has the following approximation and superconvergence properties

$$(4.10) \quad \|\eta\|_{H^m(K_{i,j})} \leq Ch^{k+1-m}|w|_{H^{k+1}(K_{i,j})} \quad \forall 0 \leq m \leq k+1,$$

$$(4.11) \quad |\mathcal{H}(\eta, v)| \leq Ch^{k+1} \|v\| \quad \forall v \in \mathbb{V}^k.$$

The second inequality is the Cauchy–Schwarz version of [23, (2.30)]. It can be obtained by first applying the Cauchy–Schwarz inequality to [23, (2.27)], then the inverse estimates [23, (2.20)], next the approximation estimates [23, (2.19)], and finally the Bramble–Hilbert lemma.

Unified notations for both 1D and 2D cases. The OEDG scheme for (4.1) in 1D and in 2D for Cartesian meshes can be written in the following unified form

$$(4.12a) \quad \left(u_h^{n,\ell+1}, v \right) = \sum_{0 \leq m \leq \ell} \left(c_{\ell m} (u_\sigma^{n,m}, v) + \tau d_{\ell m} (\mathcal{H}(u_\sigma^{n,m}, v) + (g^{n,m}, v)) \right),$$

$$(4.12b) \quad u_\sigma^{n,\ell+1} = \mathcal{F}_\tau u_h^{n,\ell+1}, \quad 0 \leq \ell \leq s-1,$$

and the OE step corresponding to the solution of

$$(4.13) \quad \begin{cases} \frac{d}{dt} (u_\sigma, v)_K + \sum_{m=0}^k \delta_K^m (u_\sigma - P^{m-1} u_\sigma, v)_K = 0 \quad \forall v \in \mathbb{P}^k(K), \\ u_\sigma(x, 0) = u_h^{n,\ell+1}(x). \end{cases}$$

Here $K = I_j$ and $\delta_K^m = \delta_K^m(u_h^{n,\ell+1}) = \beta_j \sigma_j^m (u_h^{n,\ell+1})/h_j$ for the 1D case; $K = K_{i,j}$ and δ_K^m is defined in (3.9), or more specifically in (3.12), for the 2D case.

The projection P^* for the error estimates, is defined as the Gauss–Radau projection in (4.4) for the 1D case, and the Liu–Shu–Zhang projection in (4.8) for the 2D case. For both cases, with $\eta = w - P^*w$, we have

$$(4.14a) \quad \|\eta\|_{H^m(K)} \leq Ch^{k+1-m} |w|_{H^{k+1}(K)} \quad \forall 0 \leq m \leq k+1,$$

$$(4.14b) \quad |\mathcal{H}(\eta, v)| \leq Ch^{k+1} \|v\| \quad \forall v \in \mathbb{V}^k.$$

Note that, in particular, (4.14a) implies $\|\eta\| \leq Ch^{k+1}$.

The following estimates, which hold for all $v \in \mathbb{P}^k(K)$, will be used in our analysis.

$$(4.15a) \quad \|v\|_{H^1(K)} \leq Ch^{-1} \|v\|_{L^2(K)},$$

$$(4.15b) \quad \|v\|_{L^2(\partial K)} \leq Ch^{-\frac{1}{2}} \|v\|_{L^2(K)},$$

$$(4.15c) \quad \|v\|_{L^\infty(K)} \leq Ch^{-\frac{d}{2}} \|v\|_{L^2(K)}.$$

Note that applying the first two inequalities to (4.3) and (4.7) gives

$$(4.16) \quad |\mathcal{H}(w, v)| \leq Ch^{-1} \|w\| \|v\| \quad \forall w, v \in \mathbb{V}^k.$$

4.2.2. Stability of the RKDG method. The error estimate will be built upon the stability of the original RKDG method for the nonhomogeneous equation (4.1) without the OE step. For ease of presentation, we first state the stability as a general assumption in Assumption 4.5, and then state in Proposition 4.6 on stability of the r th-order r -stage RKDG methods for linear equations.

ASSUMPTION 4.5 (Stability of the RKDG method). *Under the time step constraint $\tau \leq C_{\text{CFL}} h^\kappa$ with $\kappa \geq 1$, the RKDG method without the OE procedure, namely (4.12) with $\mathcal{F}_\tau \equiv \mathcal{I}$, satisfies*

$$(4.17) \quad \|u_h^{n+1}\|^2 \leq (1 + C_s \tau) \|u_h^n\|^2 + C\tau \sum_{0 \leq \ell < s} \|g^{n,\ell}\|^2.$$

Proposition 4.6 is collected from [35]. See also [30, 31, 37, 32] for related results. Most of these works focus on the case $g \equiv 0$, but the extension to $g \not\equiv 0$ is straight forward. See for example, [36], for the case of the classical fourth-order RK method. General stability criteria of an arbitrary RK method can also be found in the aforementioned literature.

PROPOSITION 4.6. *Consider an r th-order r -stage RK method for linear problems.*

1. *If $r \equiv 1 \pmod{4}$, then Assumption 4.5 holds with $\kappa = 1 + 1/r$.*
2. *If $r \equiv 2 \pmod{4}$, then Assumption 4.5 holds with $\kappa = 1 + 1/(r+1)$.*
3. *If $r \equiv 3 \pmod{4}$, then Assumption 4.5 holds with $\kappa = 1$ and $C_s = 0$.*
4. *If $r \equiv 0 \pmod{4}$, then after combining every 2 or 3 time steps as a single step and renumbering the stages, Assumption 4.5 holds with $\kappa = 1$ and $C_s = 0$.*

4.2.3. Reference functions. We will only consider $g \equiv 0$ in (2.3) in our error estimates. We introduce the reference solution $U^{n,0} = u(x, t^n)$ and define recursively

$$(4.18) \quad (U^{n,\ell+1}, v) = \sum_{0 \leq m \leq \ell} (c_{\ell m} (U^{n,m}, v) + \tau d_{\ell m} \mathcal{H}(U^{n,m}, v)) + \tau (\rho^{n,\ell}, v) \quad \text{for } 0 \leq \ell \leq s-1.$$

Here $\rho^{n,\ell} \equiv 0$ for $\ell < s-1$ and $\rho^{n,s-1}$ is set so that $U^{n,s} = u(x, t^{n+1}) = U^{n+1,0}$. As a convention, $U^n := U^{n,0}$. With a Taylor expansion, it can be shown that

$$(4.19) \quad \|\rho^{n,s-1}\| \leq C\tau^r.$$

Remark 4.7. Since $U^{n,m}$ is smooth, we have $\mathcal{H}(U^{n,m}, v) = -(\beta \cdot \nabla U^{n,m}, v)$. Hence it can be seen from (4.18) that we need $u(\cdot, t) \in H^s(\Omega)$ to ensure all $U^{n,\ell}$ and $\rho^{n,\ell}$ are well defined. But

typically, we expect the required regularity of u to be close to r instead of s . This could lead to very restrictive regularity condition on u for some RK schemes with $s \gg r$, or in the case $s = r$ and $r \equiv 0 \pmod{4}$, for which we combine multiple time steps in the stability estimate. The dependence of the regularity condition on s can be avoided by carefully truncating the high-order terms in the definition of $U^{n,m}$. This more sophisticated choice of $U^{n,\ell}$ will recover the minimum regularity requirement on u . We refer to [35, Section 4.1.2] and [36, Section 5.2] for details, and refrain from pursuing it here for simplicity.

4.3. Proof of Theorem 4.1. For simplicity, we assume that $h \leq 1$ and $\tau \leq 1$ are sufficiently small. The route map of the fully discrete error analysis is outlined as follows.

1. We make an a priori assumption for all $0 \leq n \leq n_*$ and $1 \leq \ell \leq s$,

$$(4.20) \quad \|\xi^{n,\ell}\|_{L^\infty(\Omega)} := \|u_h^{n,\ell} - P^*U^{n,\ell}\|_{L^\infty(\Omega)} \leq h.$$

We prove Theorem 4.1 under this assumption through the following steps.

- (a) We rewrite the OEDG scheme and its corresponding error equation in the form of an RKDG scheme with a source term at each stage.
 - (b) We show that these additional source terms are small and high-order terms.
 - (c) The steps outline above lead to an error equation within a single time step. We then apply the discrete Grönwall's inequality to prove the global-in-time error estimates.
2. We prove the a priori assumption (4.20) inductively.

Now, we will provide the proof of Theorem 4.1. The proofs of the associated lemmas will be deferred to the next section. As previously stated, Steps 1 requires the assumption (4.20), which is used in Lemma 4.9 at Step 1(b).

Step 1(a). Set $g^{n,m} \equiv 0$ and add $(u_\sigma^{n,\ell+1} - u_h^{n,\ell+1}, v)$ on both sides of (4.12a). It yields

$$(4.21) \quad (u_\sigma^{n,\ell+1}, v) = \sum_{0 \leq m \leq \ell} (c_{\ell m} (u_\sigma^{n,m}, v) + \tau d_{\ell m} \mathcal{H}(u_\sigma^{n,m}, v)) + (u_\sigma^{n,\ell+1} - u_h^{n,\ell+1}, v),$$

for $0 \leq \ell \leq s-1$. We define

$$(4.22) \quad \xi_\sigma^{n,m} = u_\sigma^{n,m} - P^*U^{n,m}, \quad \xi_h^{n,m} = u_h^{n,m} - P^*U^{n,m} \quad \text{and} \quad \eta^{n,m} = U^{n,m} - P^*U^{n,m}.$$

Subtracting (4.18) from (4.21) gives

$$(4.23) \quad (\xi_\sigma^{n,\ell+1}, v) = \sum_{0 \leq m \leq \ell} (c_{\ell m} (\xi_\sigma^{n,m}, v) + \tau d_{\ell m} \mathcal{H}(\xi_\sigma^{n,m}, v)) + \tau \mathcal{Y}^{n,\ell}(v) + \tau \mathcal{Z}^{n,\ell}(v),$$

where

$$(4.24) \quad \mathcal{Y}^{n,\ell}(v) = \tau^{-1} (u_\sigma^{n,\ell+1} - u_h^{n,\ell+1}, v),$$

$$(4.25) \quad \mathcal{Z}^{n,\ell}(v) = (\eta_c^{n,\ell}, v) - \mathcal{H}(\eta_d^{n,\ell}, v) - (\rho^{n,\ell}, v),$$

with

$$(4.26) \quad \eta_c^{n,\ell} = \tau^{-1} \left(\eta^{n,\ell+1} - \sum_{0 \leq m \leq \ell} c_{\ell m} \eta^{n,m} \right) \quad \text{and} \quad \eta_d^{n,\ell} = \sum_{0 \leq m \leq \ell} d_{\ell m} \eta^{n,m}.$$

To apply the stability estimate in Assumption 4.5, we rewrite (4.23) as

$$(4.27) \quad (\xi_\sigma^{n,\ell+1}, v) = \sum_{0 \leq m \leq \ell} (c_{\ell m} (\xi_\sigma^{n,m}, v) + \tau d_{\ell m} (\mathcal{H}(\xi_\sigma^{n,m}, v) + (G^{n,m}, v))), \quad 0 \leq \ell \leq s-1.$$

Here $G^{n,m}$ is defined inductively as

$$(4.28) \quad d_{\ell\ell}(G^{n,\ell}, v) = \mathcal{Y}^{n,\ell}(v) + \mathcal{Z}^{n,\ell}(v) - \sum_{0 \leq m \leq \ell-1} d_{\ell m}(G^{n,m}, v), \quad 0 \leq \ell \leq s-1.$$

Step 1(b). From the definition of $G^{n,\ell}$ in (4.28), one can see that

$$(4.29) \quad \|G^{n,\ell}\| \leq C \sum_{0 \leq m \leq \ell} (\|\mathcal{Y}^{n,m}\| + \|\mathcal{Z}^{n,m}\|).$$

Here $\|\mathcal{Y}^{n,m}\| = \sup_{v \in \mathbb{V}^k, v \neq 0} \frac{\|\mathcal{Y}^{n,m}(v)\|}{\|v\|}$ and $\|\mathcal{Z}^{n,m}\| = \sup_{v \in \mathbb{V}^k, v \neq 0} \frac{\|\mathcal{Z}^{n,m}(v)\|}{\|v\|}$. Consequently, to estimate the norm of the source term $G^{n,\ell}$, we require estimates of $\|\mathcal{Z}^{n,\ell}\|$ and $\|\mathcal{Y}^{n,\ell}\|$, which are provided below. Their proofs will be postponed to Subsection 4.4.1 and Subsection 4.4.3, respectively.

LEMMA 4.8. $\|\mathcal{Z}^{n,\ell}\| \leq C(h^{k+1} + \tau^r)$.

LEMMA 4.9. *If $\|\xi^{n,m}\|_{L^\infty(\Omega)} \leq h$ for all $1 \leq m \leq \ell + 1$, then*

$$(4.30) \quad \|\mathcal{Y}^{n,\ell}\| \leq C(\|\xi_\sigma^n\| + h^{k+1} + \tau^r).$$

Applying Lemma 4.8 and Lemma 4.9 in (4.29) yields

$$(4.31) \quad \|G^{n,\ell}\| \leq C(\|\xi_\sigma^n\| + h^{k+1} + \tau^r).$$

Step 1(c). From (4.27), we see that $\xi_\sigma^{n,\ell}$ satisfies the RKDG scheme accompanied by the source term $G^{n,\ell}$. Apply the stability result (4.17) to (4.27) and use the estimate (4.31). It gives

$$(4.32) \quad \|\xi_\sigma^{n+1}\|^2 \leq (1 + C_s \tau) \|\xi_\sigma^n\|^2 + C\tau \sum_{0 \leq \ell < s} \|G^{n,\ell}\|^2 \leq (1 + C\tau) \|\xi_\sigma^n\|^2 + C\tau(h^{2k+2} + \tau^{2r}).$$

Since constants in (4.32) are independent of n , one can apply the discrete Grönwall's inequality to get

$$(4.33) \quad \|\xi_\sigma^n\|^2 \leq C_\star^2 \left(\|\xi_\sigma^0\|^2 + h^{2k+2} + \tau^{2r} \right) \quad \forall 0 \leq n \leq n_\star.$$

Here we address that C_\star is a constant that is independent of h , τ , n , and n_\star , but may depend on the final time $T = n_\star \tau$. Then applying the inequality $\sqrt{a^2 + b^2 + c^2} \leq |a| + |b| + |c|$ gives

$$(4.34) \quad \|\xi_\sigma^n\| \leq C_\star (\|\xi_\sigma^0\| + h^{k+1} + \tau^r) \quad \forall 0 \leq n \leq n_\star.$$

Recall that $u_\sigma^i - u(x, t^i) = \xi_\sigma^i - \eta^i$ with $i = 0, n$. We can use the triangle inequality, the approximation property of P^\star , the fact $\|u_\sigma^0 - u(\cdot, 0)\| \leq Ch^{k+1}$, to get

$$(4.35) \quad \|u_\sigma^n - u(\cdot, n\tau)\| \leq C_\star (h^{k+1} + \tau^r) \quad \forall 0 \leq n \leq n_\star.$$

The proof of Theorem 4.1, under the assumption (4.20), can be completed by maximizing both sides over n and observing the independence of C_\star from n .

Step 2. Note we have the following lemma, whose proof will be given in Subsection 4.4.4.

LEMMA 4.10. *Suppose $k > \frac{d}{2}$ and $r > \frac{d}{2} + 1$. If $\|\xi_\sigma^n\| \leq C_{\star\star}(h^{k+1} + \tau^r)$, then $\|\xi_\sigma^{n,\ell}\| \leq C(h^{k+1} + \tau^r)$ and $\|\xi^{n,\ell}\|_{L^\infty(\Omega)} \leq h$ for all $1 \leq \ell \leq s$ under the assumption $h \leq \bar{C}_{\star\star}$. Here $\bar{C}_{\star\star}$ is a fixed constant dependent on $C_{\star\star}$.*

Now we verify the a priori assumption (4.20).

Let us fix the constant C_\star in (4.34), which is obtained in Step 1 under the a priori assumption (4.20) and appears in the bound of $\|\xi_\sigma^n\|$ for all $0 \leq n \leq n_\star$. By the choice of the initial data, we have $\|\xi_\sigma^0\| \leq C_\star h^{k+1}$. Without loss of generality, we assume $C_\star > 1$ and $C_\star > 1$ and define $C_{\star\star} = C_\star(C_\star + 1)$. According to Lemma 4.10, since $\|\xi_\sigma^0\| \leq C_{\star\star}(h^{k+1} + \tau^r)$, the a priori assumption

(4.20) holds for $n = 0$ and all $1 \leq \ell \leq s$ when $h \leq \overline{C}_{**}$. Thus one can follow the argument in Step 1 and apply the discrete Grönwall's inequality to get (4.34) with $n = 1$, which can be elaborated as

$$(4.36) \quad \|\xi_\sigma^1\| \leq C_* (\|\xi_\sigma^0\| + h^{k+1} + \tau^r) \leq C_*(C_* + 1)(h^{k+1} + \tau^r) = C_{**}(h^{k+1} + \tau^r).$$

Now the assumption in Lemma 4.10 becomes valid for $n = 1$. Hence one can conclude that the a priori assumption (4.20) holds for $n = 1$ and all $1 \leq \ell \leq s$ under the same prescribed condition $h \leq \overline{C}_{**}$. Then one can continue further as that in Step 1 and apply discrete Grönwall's inequality to $n = 2$ to obtain

$$(4.37) \quad \|\xi_\sigma^2\| \leq C_* (\|\xi_\sigma^0\| + h^{k+1} + \tau^r) \leq C_{**}(h^{k+1} + \tau^r).$$

Thus by Lemma 4.10, the a priori assumption holds for $n = 2$. This argument can be further continued and formalized by induction to show that $\|\xi_\sigma^n\| \leq C_{**}(h^{k+1} + \tau^r)$, and the a priori assumption $\|\xi_\sigma^{n,\ell}\|_{L^\infty(\Omega)} \leq h$ holds for all $0 \leq n \leq n_*$ and $1 \leq \ell \leq s$, if $h \leq \overline{C}_{**}$. This validates the a priori assumption (4.20) and thus completes the proof of Theorem 4.1.

4.4. Proofs of lemmas. It now remains to prove the lemmas used in the proof of Theorem 4.1.

4.4.1. Proof of Lemma 4.8. This lemma is a special case of [35, Lemma 4.6] with $q = 0$. Recall the definition in (4.25). One can use the definition of $\rho^{n,\ell}$ in Subsection 4.2.3 to get $|(\rho^{n,\ell}, v)| \leq C\tau^r \|v\|$, and the superconvergence property in (4.14b) to show $|\mathcal{H}(\eta_d, v)| \leq Ch^{k+1} \|v\|$. Let $W_c^{n,\ell} = U^{n,\ell+1} - \sum_{0 \leq m \leq \ell} c_{\ell m} U^{n,m}$. Note that, from (4.18),

$$(4.38) \quad (W_c^{n,\ell}, v) = \tau \left(- \sum_{0 \leq m \leq \ell} d_{\ell,m} \boldsymbol{\beta} \cdot \nabla U^{n,\ell} + \rho^{n,\ell}, v \right) := \tau (w^{n,\ell}, v).$$

Hence $(\eta_c^{n,\ell}, v) = \tau^{-1} (W_c^{n,\ell} - P^* W_c^{n,\ell}, v) = (w^{n,\ell} - P^* w^{n,\ell}, v)$. Then by the approximation property in (4.14a), we have $|(\eta_c^{n,\ell}, v)| \leq Ch^{k+1} \|v\|$. The proposition can be proven after combining the three inequalities of $|(\rho^{n,\ell}, v)|$, $|\mathcal{H}(\eta_d, v)|$, and $|(\eta_c^{n,\ell}, v)|$.

4.4.2. Preparations for Lemma 4.9 and Lemma 4.10. Before proving the remaining lemmas in Subsection 4.3, we need to introduce two preparatory lemmas, Lemma 4.11 and Lemma 4.14. Lemma 4.12 and Lemma 4.13 are used solely for proving Lemma 4.14 and will not be used elsewhere.

LEMMA 4.11. $\|\xi_\sigma^{n,\ell+1}\| \leq C \left(\sum_{0 \leq m \leq \ell} \|\xi_\sigma^{n,m}\| \right) + C\tau (h^{k+1} + \tau^r)$ for $0 \leq \ell \leq s-1$.

Proof. Combining (4.23) and (4.24), it yields

$$(4.39) \quad \begin{aligned} (\xi_\sigma^{n,\ell+1}, v) &= \sum_{0 \leq m \leq \ell} (c_{\ell m} (\xi_\sigma^{n,m}, v) + \tau d_{\ell m} \mathcal{H}(\xi_\sigma^{n,m}, v)) + \tau \mathcal{Z}^{n,\ell}(v) \\ &\leq \sum_{0 \leq m \leq \ell} (|c_{\ell m}| \|\xi_\sigma^{n,m}\| \|v\| + C\tau h^{-1} \|\xi_\sigma^{n,m}\| \|v\|) + \tau \|\mathcal{Z}^{n,\ell}\| \|v\| \\ &\leq C \left(\sum_{0 \leq m \leq \ell} \|\xi_\sigma^{n,m}\| + \tau \|\mathcal{Z}^{n,\ell}\| \right) \|v\|. \end{aligned}$$

Here we have used the estimate (4.16) and the time step constraint $\tau h^{-1} \leq C_{\text{CFL}} h^{k-1} \leq C_{\text{CFL}}$. After taking $v = \xi_\sigma^{n,\ell+1}$ and applying the estimate of $\|\mathcal{Z}^{n,\ell}\|$ in Lemma 4.8, we complete the proof of Lemma 4.11. \square

LEMMA 4.12. $|\delta_K^n(u_h^{n,\ell+1})| \leq C \left(h^{-1-\frac{d}{2}} \|\xi_\sigma^{n,\ell+1}\|_{L^2(K)} + h^{k-\frac{d}{2}} \|U^{n,\ell+1}\|_{H^{k+1}(K)} \right)$.

Proof. We omit the superscript $(n, \ell + 1)$ and denote by $w := w^{n,\ell+1}$ with $w = u_h, \xi, \eta, U$ in this proof. We adopt the general notations in (3.9) and (3.10) to prove the general case. The proof of the

1D case is similar and is hence omitted. Recall that $\|u_h - \text{avg}(u_h)\|_{L^\infty(\Omega)} \geq C > 0$ and $|\beta_e| \leq C$ for our linear advection equation. Hence with (3.9) and (3.10), we have

$$(4.40) \quad (\delta_K^m)^2 = \left(\sum_{e \in \partial K} \frac{\beta_e}{h_{e,K}} \frac{(2m+1)h_{e,K}^m}{2(2k-1)m!} \sum_{|\alpha|=m} \frac{\frac{1}{|e|} \int_e |[\partial^\alpha u_h]_e| dS}{\|u_h - \text{avg}(u_h)\|_{L^\infty(\Omega)}} \right)^2 \\ \leq C \sum_{e \in \partial K} \sum_{|\alpha|=m} h^{2m-2} \left(\frac{1}{|e|} \int_e |[\partial^\alpha u_h]_e| dS \right)^2.$$

With the Cauchy–Schwarz inequality, the fact $[[u_h]] = [[\xi - \eta + U]] = [[\xi]] - [[\eta]]$, and the inequality $(a+b)^2 \leq 2a^2 + 2b^2$, we have

$$(4.41) \quad \left(\frac{1}{|e|} \int_e |[\partial^\alpha u_h]_e| dS \right)^2 \leq \frac{1}{|e|} \int_e |[\partial^\alpha u_h]_e|^2 dS \leq Ch^{-(d-1)} \left(\int_e |[\partial^\alpha \xi]_e|^2 dS + \int_e |[\partial^\alpha \eta]_e|^2 dS \right).$$

Substituting it into (4.40) yields

$$(4.42) \quad (\delta_K^m)^2 \leq C \sum_{|\alpha|=m} \sum_{e \in \partial K} h^{2m-1-d} \left(\int_e |[\partial^\alpha \xi]_e|^2 dS + \int_e |[\partial^\alpha \eta]_e|^2 dS \right).$$

With the multiplicative trace inequality (see, e.g., [11, Lemma 3.1]) and the inverse estimates, it yields

$$(4.43) \quad \sum_{e \in \partial K} \int_e |[\partial^\alpha \xi]_e|^2 dS \leq C \|\partial^\alpha \xi\|_{L^2(K)} \left(\|\partial^\alpha \xi\|_{H^1(K)} + h^{-1} \|\partial^\alpha \xi\|_{L^2(K)} \right) \leq Ch^{2m-1} \|\xi\|_{L^2(K)}^2.$$

Similarly, using the approximation property of P^* , it yields

$$(4.44) \quad \sum_{e \in \partial K} \int_e |[\partial^\alpha \eta]_e|^2 dS \leq C \|\partial^\alpha \eta\|_{L^2(K)} \left(\|\partial^\alpha \eta\|_{H^1(K)} + h^{-1} \|\partial^\alpha \eta\|_{L^2(K)} \right) \leq Ch^{2k+1-2m} \|U\|_{H^{k+1}(K)}^2.$$

Substituting (4.43) and (4.44) into (4.42), it yields

$$(4.45) \quad (\delta_K^m)^2 \leq C \left(h^{-d-2} \|\xi\|_{L^2(K)}^2 + h^{2k-d} \|U\|_{H^{k+1}(K)}^2 \right).$$

The proof is completed after taking a square root on both sides and noting that $\sqrt{a^2 + b^2} \leq |a| + |b|$. \square

LEMMA 4.13. *If $\|\xi^{n,\ell+1}\|_{L^\infty(\Omega)} \leq h$, then $\|u_h^{n,\ell+1} - P^{m-1}u_h^{n,\ell+1}\|_{L^2(K)} \leq Ch^{1+\frac{d}{2}}$, for $0 \leq m \leq k$.*

Proof. We omit the superscript $(n, \ell + 1)$ and denote by $w := w^{n,\ell+1}$ with $w = u_h, \xi, \eta, U$ in this proof. Recall $u_h = \xi - \eta + U$. With $\|I - P^{m-1}\|_{L^2(K)} \leq 1$ and the triangle inequality, we have

$$(4.46) \quad \|u_h - P^{m-1}u_h\|_{L^2(K)} = \|(I - P^{m-1})(\xi - \eta + U)\|_{L^2(K)} \\ \leq \|\xi\|_{L^2(K)} + \|\eta\|_{L^2(K)} + \|(I - P^{m-1})U\|_{L^2(K)} \\ \leq \|\xi\|_{L^2(K)} + Ch^{\max(1,m)+\frac{d}{2}} \leq \|\xi\|_{L^\infty(K)} h^{\frac{d}{2}} + Ch^{1+\frac{d}{2}}.$$

Here we have used the approximation property of P^* and P^{m-1} in $L^2(K)$ in the second last inequality. The proof is then completed after applying the a priori assumption (4.20). \square

LEMMA 4.14. *If $\|\xi^{n,\ell+1}\|_{L^\infty(\Omega)} \leq h$, then $\|u_\sigma^{n,\ell+1} - u_h^{n,\ell+1}\| \leq C\tau (\|\xi^{n,\ell+1}\| + h^{k+1})$.*

Proof. We omit the superscripts $(n, \ell + 1)$ and denote by $w := w^{n,\ell+1}$ with $w = u_h, u_\sigma, \xi$ in this section. Note that u_h is independent of \hat{t} . The OE procedure (4.13), with the unknown $u_\sigma = u_\sigma(x, \hat{t})$, can be written as

$$(4.47) \quad ((u_\sigma - u_h)_{\hat{t}}, v)_K + \sum_{m=0}^k \delta_K^m (u_\sigma - u_h - P^{m-1}(u_\sigma - u_h), v)_K = - \sum_{m=0}^k \delta_K^m (u_h - P^{m-1}u_h, v)_K.$$

Since $(v - P^{m-1}v, P^{m-1}v)_K = 0$, we can take $v = u_\sigma - u_h$ to obtain

$$(4.48) \quad \begin{aligned} \frac{1}{2} \frac{d}{d\hat{t}} \|u_\sigma - u_h\|_{L^2(K)}^2 + \sum_{m=0}^k \delta_K^m \|u_\sigma - u_h - P^{m-1}(u_\sigma - u_h)\|_{L^2(K)}^2 \\ = - \sum_{m=0}^k \delta_K^m (u_h - P^{m-1}u_h, u_\sigma - u_h)_K. \end{aligned}$$

Drop the second term on the left and apply the Cauchy–Schwarz inequality on the right. After canceling $\|u_\sigma - u_h\|_{L^2(K)}$ on both sides, it gives

$$(4.49) \quad \frac{d}{d\hat{t}} \|u_\sigma - u_h\|_{L^2(K)} \leq \sum_{m=0}^k |\delta_K^m| \|u_h - P^{m-1}u_h\|_{L^2(K)}.$$

After applying Lemma 4.13 and Lemma 4.12 in (4.49), we get

$$(4.50) \quad \frac{d}{d\hat{t}} \|u_\sigma - u_h\|_{L^2(K)} \leq C \left(\|\xi\|_{L^2(K)} + h^{k+1} \|U\|_{H^{k+1}(K)} \right).$$

Note the right hand is independent of \hat{t} . After integrating the inequality from $\hat{t} = 0$ to $\hat{t} = \tau$ and using the initial condition $u_\sigma(\cdot, 0) = u_h(\cdot)$, we get

$$(4.51) \quad \|u_\sigma - u_h\|_{L^2(K)} \leq C\tau \left(\|\xi\|_{L^2(K)} + h^{k+1} \|U\|_{H^{k+1}(K)} \right).$$

The proof of Lemma 4.14 can be completed after taking the square on both sides of (4.51), summing over all K , taking a square root, and finally applying the inequality $\sqrt{a^2 + b^2} \leq |a| + |b|$. \square

4.4.3. Proof of Lemma 4.9. Note that $\xi_\sigma^{n,\ell+1} = \xi^{n,\ell+1} + (u_\sigma^{n,\ell+1} - u_h^{n,\ell+1})$. Apply the triangle inequality, Lemma 4.14, and then Lemma 4.11. It gives

$$(4.52) \quad \begin{aligned} \|\xi_\sigma^{n,\ell+1}\| &\leq \|\xi^{n,\ell+1}\| + \|u_\sigma^{n,\ell+1} - u_h^{n,\ell+1}\| \leq C \|\xi^{n,\ell+1}\| + C\tau h^{k+1} \\ &\leq C \sum_{0 \leq m \leq \ell} \|\xi_\sigma^{n,m}\| + C\tau (h^{k+1} + \tau^r). \end{aligned}$$

Hence by induction, we have

$$(4.53) \quad \|\xi_\sigma^{n,m}\| \leq C \|\xi_\sigma^n\| + C\tau (h^{k+1} + \tau^r) \quad \forall 0 \leq m \leq \ell + 1.$$

Substituting (4.53) into Lemma 4.11 yields

$$(4.54) \quad \|\xi^{n,\ell+1}\| \leq C \|\xi_\sigma^n\| + C\tau (h^{k+1} + \tau^r).$$

Together with Lemma 4.14, one can get

$$(4.55) \quad \|\mathcal{Y}^{n,\ell}\| = \tau^{-1} \|u_\sigma^{n,\ell+1} - u_h^{n,\ell+1}\| \leq C (\|\xi_\sigma^n\| + h^{k+1} + \tau^r).$$

4.4.4. Proof of Lemma 4.10. For convenience, we define $\xi^{n,0} = \xi_\sigma^n$. For $\ell = 0$, note we automatically get $\|\xi_\sigma^{n,0}\| = \|\xi_\sigma^n\| \leq C_{**} (h^{k+1} + \tau^r)$. Since $\tau \leq C_{\text{CFL}} h^\kappa$, by (4.15c), we have

$$(4.56) \quad \|\xi_\sigma^{n,0}\|_{L^\infty(\Omega)} \leq Ch^{-\frac{d}{2}} \|\xi_\sigma^{n,0}\| = Ch^{-\frac{d}{2}} \|\xi_\sigma^n\| \leq C_0 h^{\min(k+1-\frac{d}{2}, r\kappa-\frac{d}{2})} \leq h$$

if $h \leq C_0^{-1/(\min(k,r-1)-d/2)}$. Hence the lemma holds for $\ell = 0$.

Now assume the lemma is true for all $m \leq \ell$ under the assumption $h \leq \min_{0 \leq m \leq \ell} C_m^{-1/(\min(k,r-1)-d/2)}$. By Lemma 4.11 and the induction hypothesis, we have

$$(4.57) \quad \|\xi^{n,\ell+1}\| \leq C (h^{k+1} + \tau^r).$$

Thus using (4.15c), we have

$$(4.58) \quad \|\xi^{n,\ell+1}\|_{L^\infty(\Omega)} \leq Ch^{-\frac{d}{2}} \|\xi^{n,\ell+1}\| \leq C_{\ell+1} h^{\min(k+1-\frac{d}{2}, r\kappa-\frac{d}{2})} \leq h$$

if $h \leq C_{\ell+1}^{-1/(\min(k,r-1)-d/2)}$. Hence with this extra constraint, the assumption in Lemma 4.14 becomes valid and the lemma gives

$$(4.59) \quad \left\| u_\sigma^{n,\ell+1} - u_h^{n,\ell+1} \right\| \leq C\tau (h^{k+1} + \tau^r).$$

Applying the triangle inequality, (4.57), and (4.59), it yields

$$(4.60) \quad \|\xi_\sigma^{n,\ell+1}\| \leq \|\xi^{n,\ell+1}\| + \left\| u_\sigma^{n,\ell+1} - u_h^{n,\ell+1} \right\| \leq C(h^{k+1} + \tau^r).$$

With (4.58) and (4.60), the lemma is proven for $m = \ell + 1$ with $h \leq \min_{0 \leq m \leq \ell+1} C_m^{-1/(\min(k,r-1)-d/2)}$. The proof is completed by induction.

So far, all lemmas in Subsection 4.3 are proven, and the proof of Theorem 4.1 is now complete.

5. Numerical tests. This section presents extensive 1D and 2D benchmark numerical examples to validate the theoretical analysis and to demonstrate the accuracy, effectiveness, and robustness of the proposed OEDG method. The examples encompass four models of hyperbolic conservation laws: the linear advection equation, inviscid Burgers' equation, Lighthill–Whitham–Richards traffic flow model, and compressible Euler equations. Unless stated otherwise, for smooth problems, we employ a $(k+1)$ th-order explicit RK time discretization for the \mathbb{P}^k -based OEDG method to validate the optimal convergence rates; for problems involving discontinuities, we typically use the classic third-order strong-stability-preserving explicit RK time discretization. The OEDG method remains stable under the normal CFL condition, thanks to the exact solver for the OE step. Consequently, we set the time stepsize as $\Delta t = C_{\text{CFL}} h / \beta$ for 1D problems, where β represents the maximum wave speed, and the CFL number $C_{\text{CFL}} = \frac{1}{2k+1}$ for the \mathbb{P}^k -based OEDG method. Analogously, for 2D problems on uniform rectangular meshes with spatial stepsizes h_x and h_y , we adopt $\Delta t = C_{\text{CFL}} / (\beta_x/h_x + \beta_y/h_y)$. To demonstrate the importance of scale-invariant and evolution-invariant properties, we will compare the proposed OEDG method with the OFDG method [24, 21], which is coupled with a third-order exponential RK time discretization [20] to mitigate restrictive time step constraints for discontinuous problems. We adopt the upwind flux for linear equations and the local Lax–Friedrichs flux for the others. Both OEDG and OFDG methods are implemented in C/C++ with double precision.

5.1. 1D linear advection equation. We consider two examples of the advection equation on the spatial domain $\Omega = [0, 1]$ with periodic boundary conditions.

Example 5.1 (smooth problem). The first example is used to validate the optimal convergence rates and explore the superconvergence by solving the equation $u_t + u_x = 0$ with the initial condition $u_0(x) = \sin^2(2\pi x)$ up to time $t = 1.1$. We measure the following five types of numerical errors:

$$e_1 := \|u - u_h\|_{L^1(\Omega)}, \quad e_2 := \|u - u_h\|_{L^2(\Omega)}, \quad e_3 := \|u - u_h\|_{L^\infty(\Omega)},$$

$$e_4 := \left(h \sum_j \left| \frac{1}{h} \int_{I_j} (u - u_h) dx \right|^2 \right)^{\frac{1}{2}}, \quad e_5 := \left(h \sum_j \left| u(x_{j+\frac{1}{2}}) - u_{h,j+\frac{1}{2}}^- \right|^2 \right)^{\frac{1}{2}}.$$

To verify the optimal convergence rates of e_1 , e_2 , and e_3 , we employ a $(k+1)$ th-order explicit RK time discretization for the \mathbb{P}^k -based OEDG method. For the investigation of superconvergence phenomena related to e_4 and e_5 , we alternatively use a seventh-order RK method and follow [24] to initialize $u_h(x, 0) = P^* u_0(x)$ by using the Gauss–Radau projection P^* in (4.4). Table 1 lists the numerical errors at $t = 1.1$ for the OEDG method with N_x uniform cells. Note that on coarse meshes, the high-order damping effect dominates the numerical errors, resulting in convergence rates higher than $k+1$, a phenomenon also observed in the OFDG method [24]. For comparison, Table 2 gives the error table

of the conventional DG method under the same settings but without the OE procedure. Our results demonstrate the optimal convergence rates in three different norms (e_1 , e_2 , and e_3), thereby confirming the fully discrete error analysis in Section 4. We also observe the $(k + 2)$ th-order superconvergence in e_4 and e_5 . The same superconvergence phenomena were also observed and proven for the semidiscrete OFDG method [24], but the rigorous proof is currently lacking for the fully discrete OEDG method and will be explored in the future work.

Table 1: Errors and convergence rates for \mathbb{P}^k -based OEDG method at different mesh resolutions.

k	N_x	e_1	rate	e_2	rate	e_3	rate	e_4	rate	e_5	rate
1	128	1.69e-3	-	1.96e-3	-	3.62e-3	-	2.06e-3	-	2.07e-3	-
	256	2.81e-4	2.59	3.38e-4	2.54	6.14e-4	2.56	2.85e-4	2.85	2.86e-4	2.85
	512	5.96e-5	2.24	6.78e-5	2.32	1.17e-4	2.39	3.72e-5	2.94	3.73e-5	2.94
	1024	1.52e-5	1.97	1.70e-5	1.99	2.98e-5	1.98	4.73e-6	2.97	4.74e-6	2.97
	2048	3.69e-6	2.05	4.10e-6	2.05	7.02e-6	2.08	5.97e-7	2.99	5.98e-7	2.99
2	128	9.85e-6	-	1.08e-5	-	2.12e-5	-	9.93e-6	-	9.97e-6	-
	256	6.53e-7	3.91	7.18e-7	3.92	1.68e-6	3.66	5.54e-7	4.16	5.56e-7	4.17
	512	5.25e-8	3.64	5.85e-8	3.62	1.61e-7	3.38	3.28e-8	4.08	3.29e-8	4.08
	1024	5.01e-9	3.39	5.68e-9	3.36	1.75e-8	3.20	2.00e-9	4.04	2.01e-9	4.04
	2048	5.41e-10	3.21	6.23e-10	3.19	2.05e-9	3.09	1.23e-10	4.02	1.24e-10	4.02
3	128	9.10e-8	-	1.02e-7	-	2.00e-7	-	1.04e-7	-	1.05e-7	-
	256	2.91e-9	4.97	3.27e-9	4.97	7.63e-9	4.71	3.30e-9	4.98	3.31e-9	4.98
	512	9.45e-11	4.94	1.09e-10	4.91	3.45e-10	4.47	1.04e-10	4.99	1.04e-10	4.99
	1024	3.33e-12	4.83	4.02e-12	4.76	1.73e-11	4.31	3.26e-12	5.00	3.28e-12	4.99

Table 2: Errors and convergence rates for \mathbb{P}^k -based conventional RKDG method without OE step.

k	N_x	e_1	rate	e_2	rate	e_3	rate
1	128	8.12e-4	-	9.02e-4	-	1.39e-3	-
	256	2.04e-4	1.99	2.27e-4	1.99	3.57e-4	1.97
	512	5.10e-5	2.00	5.67e-5	2.00	9.03e-5	1.98
	1024	1.29e-5	1.99	1.43e-5	1.99	2.28e-5	1.99
	2048	3.20e-6	2.01	3.56e-6	2.01	5.71e-6	2.00
2	128	1.93e-6	-	2.25e-6	-	7.86e-6	-
	256	2.40e-7	3.00	2.81e-7	3.00	9.88e-7	2.99
	512	3.00e-8	3.00	3.51e-8	3.00	1.24e-7	3.00
	1024	3.74e-9	3.00	4.39e-9	3.00	1.55e-8	3.00
	2048	4.68e-10	3.00	5.48e-10	3.00	1.94e-9	3.00
3	128	7.36e-9	-	9.98e-9	-	5.22e-8	-
	256	4.60e-10	4.00	6.24e-10	4.00	3.27e-9	4.00
	512	2.88e-11	4.00	3.90e-11	4.00	2.04e-10	4.00
	1024	1.74e-12	4.05	2.41e-12	4.02	1.29e-11	3.99

Example 5.2 (discontinuous problems in different scales). This example illustrates that our OEDG method is devoid of spurious oscillations and consistently displays scale invariance and evolution invariance for problems spanning different scales and wave speeds, in contrast to the OFDG method with non-scale-invariant damping (2.13). We examine the linear advection equation $u_t + \beta u_x = 0$ with discontinuous initial data described by

$$(5.1) \quad u(x, 0) = \lambda u_0(x), \quad u_0(x) := \begin{cases} \sin(2\pi x), & x \in [0.3, 0.8], \\ \cos(2\pi x) - 0.5, & \text{otherwise.} \end{cases}$$

The exact solution is given by $u(x, t) = \lambda u_0(x - \beta t)$. To assess scale invariance, we set $\beta = 1$ and vary λ within $\{1, 0.01, 100\}$, thus scaling u to represent the use of different units for u . The cell averages of the numerical solutions u_h^λ/λ at $t = 1.1$, obtained by using the third-order OEDG and OFDG schemes with 256 uniform cells, are shown in Figures 1a and 1b, respectively. As we can see, the OEDG solution consistently upholds scale invariance: $u_h^\lambda/\lambda = u_h^1$ for all λ . Such consistency allows the OEDG method to eliminate spurious oscillations effectively, irrespective of the units assigned to u . Conversely, the OFDG method with damping (2.13) lacks scale invariance, yielding varied numerical results for different λ values, as shown Figure 1b. More specifically, one can observe that the OFDG method exhibits persistent spurious oscillations (overshoots or undershoots near the discontinuity) in the small-scale case ($\lambda = 0.01$) and displays excessive smearing in the large-scale case ($\lambda = 100$). These observations are consistent with the analyses in Theorem 2.6, Theorem 2.7, and Remark 2.8.

Subsequently, we investigate the evolution-invariant attribute by fixing $\lambda = 1$ and varying wave speed $\beta \in \{1, 0.01, 100\}$, which corresponds to the use of different units for t . The numerical solutions, u_h^β , at $t = \frac{1.1}{\beta}$, obtained using the third-order OEDG and OFDG schemes with 256 uniform cells, are depicted in Figures 1c and 1d, respectively. As expected, we observe that the OEDG solution exactly satisfies the evolution invariance: $u_h^\beta(t = \frac{1.1}{\beta}) = u_h^1(t = 1.1)$ for all β . Hence, the OEDG method performs consistently well for different wave speeds. In contrast, the OFDG method is not evolution-invariant, resulting in very different numerical results for different β , as shown in Figure 1d. Specifically, the OFDG method does not fully suppress spurious oscillations (overshoots or undershoots) for $\beta = 100$ and causes serious smearing for $\beta = 0.01$. These findings, asserted by our analyses in Subsection 2.3, demonstrate the pivotal roles of scale-invariant and evolution-invariant properties in effectively eliminating spurious oscillations, thereby accentuating the superiority of the proposed OEDG method. The results of OFDG method will be improved if our new scale-invariant and evolution-invariant damping is used instead.

5.2. 1D inviscid Burgers' equation. This subsection considers the nonlinear Burgers' equation $u_t + (\frac{u^2}{2})_x = 0$ on the domain $\Omega = [0, 2\pi]$ with periodic boundary conditions.

Example 5.3 (smooth problem). We take the initial solution as $u_0(x) = \sin(x) + 0.5$ and conduct the simulation up to $t = 0.6$, during which the exact solution remains smooth. The smoothness allows us to study the convergence order of the OEDG method for such a nonlinear equation. Table 3 presents the numerical errors and corresponding convergence rates for the \mathbb{P}^k -based OEDG method with a $(k+1)$ th-order explicit RK time discretization at different mesh resolutions. We clearly observe the optimal $(k+1)$ th-order convergence order for the \mathbb{P}^k -based OEDG method. This finding suggests that the optimal convergence rates of the OEDG method are applicable to nonlinear equations as long as the solution remains smooth, even though our theoretical error estimates are solely provided for linear equations.

5.3. Lighthill—Whitham—Richards traffic flow model. This model [25] is governed by a scalar conservation law

$$(5.2) \quad u_t + f(u)_x = 0, \quad f(u) = \begin{cases} -0.4u^2 + 100u, & 0 \leq u \leq 50, \\ -0.1u^2 + 15u + 3500, & 50 \leq u \leq 100, \\ -0.024u^2 - 5.2u + 4760, & 100 \leq u \leq 350, \end{cases}$$

where t represents time in hours, x stands for distance in kilometers, and u denotes the traffic density in vehicles per kilometer (veh/km). Given the nonhomogeneous nature of $f(u)$, the exact solution operator for equation (5.2) is not homogeneous. However, the application of a scale-invariant damping operator remains pivotal. To show the importance of scale invariance and evolution invariance, we reformulate equation (5.2) in different units, resulting in the following two equivalent forms (5.3) and (5.4). Using a new time variable, $\tilde{t} = 60t$, measured in minutes, the governing equation (5.2) becomes

$$(5.3) \quad u_{\tilde{t}} + \frac{1}{60}f(u)_x = 0.$$

Table 3: Errors and convergence rates for \mathbb{P}^k -based OEDG method for 1D Burgers' equation.

k	N_x	L^1 error	rate	L^2 error	rate	L^∞ error	rate
1	64	3.09e-3	-	2.09e-3	-	4.38e-3	-
	128	6.88e-4	2.17	5.00e-4	2.06	1.11e-3	1.98
	256	1.66e-4	2.05	1.36e-4	1.87	3.36e-4	1.73
	512	4.15e-5	2.00	3.54e-5	1.95	8.76e-5	1.94
	1024	1.05e-5	1.98	9.07e-6	1.96	2.24e-5	1.97
	2048	2.67e-6	1.98	2.30e-6	1.98	5.67e-6	1.98
	4096	6.72e-7	1.99	5.81e-7	1.99	1.42e-6	1.99
	8192	1.69e-7	1.99	1.46e-7	1.99	3.57e-7	2.00
2	64	8.76e-5	-	9.75e-5	-	3.07e-4	-
	128	9.44e-6	3.21	1.06e-5	3.20	3.70e-5	3.05
	256	1.12e-6	3.08	1.28e-6	3.05	4.50e-6	3.04
	512	1.37e-7	3.03	1.58e-7	3.02	5.52e-7	3.03
	1024	1.69e-8	3.01	1.97e-8	3.01	6.90e-8	3.00
	2048	2.11e-9	3.00	2.46e-9	3.00	8.59e-9	3.00
	4096	2.64e-10	3.00	3.07e-10	3.00	1.07e-9	3.00
	8192	3.29e-11	3.00	3.84e-11	3.00	1.34e-10	3.00
3	64	2.61e-6	-	3.41e-6	-	1.14e-5	-
	128	1.34e-7	4.28	1.80e-7	4.24	6.02e-7	4.24
	256	8.10e-9	4.05	1.04e-8	4.12	3.02e-8	4.32
	512	5.16e-10	3.97	6.44e-10	4.01	1.46e-9	4.37
	1024	3.31e-11	3.96	4.08e-11	3.98	8.89e-11	4.03

By redefining the distance variable as $\tilde{x} = 1000x$ (measured in meters) and reinterpreting the density as $\tilde{u} = u/1000$ (measured in vehicles per meter, veh/m), we obtain

$$(5.4) \quad \tilde{u}_t + f(1000\tilde{u})_{\tilde{x}} = 0.$$

Example 5.4. Following [25], we simulate a traffic flow on a homogeneous freeway stretching over 20 km. Initially, the density at the entrance ($x = 0$) is set as 50 veh/km, and an accident on the freeway creates a piecewise linear traffic density profile, as depicted in [25, Figure 6]. This profile features a congestion spanning 5 km, specifically from the 10 km to 15 km measured from the entrance. To alleviate the congestion, the entrance is temporarily closed for 10 minutes. Following this closure, traffic resumes from the entrance at a heightened capacity density of 75 veh/km. However, 20 minutes later, the entrance flow reverts to its original density of 50 veh/km. At the freeway's exit, there is a traffic signal that operates on a cyclic pattern: 2 minutes of green light (indicating zero density) and 1 minute of red light (indicating jam density 350 veh/km). We perform the simulation for a duration of one hour, by solving the three equivalent governing equations (5.2), (5.3), and (5.4), respectively. Figure 2 presents the cell averages of the numerical solutions computed by the third-order OEDG and OFDG methods with 800 uniform cells in the domain $[0, 20 \text{ km}]$. The reference solution is obtained by the local Lax–Friedrichs scheme on a very fine mesh of 80,000 cells. Due to the scale-invariant and evolution-invariant attributes, the OEDG schemes for all three equations yield congruent results, devoid of any nonphysical oscillations. This stands in contrast to the OFDG method, which when integrated with damping (2.13), produces inconsistent numerical results for these three equivalent equations in varying units. Specifically, the OFDG solutions result in notable smearing for equation (5.3) and exhibit pronounced spurious oscillations in the case of equation (5.4).

5.4. 1D compressible Euler equations. This subsection considers several examples of the compressible Euler equations, which can be written in the form of (1.1) with $\mathbf{u} = (\rho, \rho v, E)^\top$ and $\mathbf{f}(\mathbf{u}) = (\rho v, \rho v^2 + p, (E + p)v)^\top$. Here ρ is the density, v is the velocity, p is the pressure, $E = \frac{1}{2}\rho v^2 + \frac{p}{\gamma - 1}$ denotes the total energy, and the adiabatic index γ is taken as 1.4 unless otherwise stated.

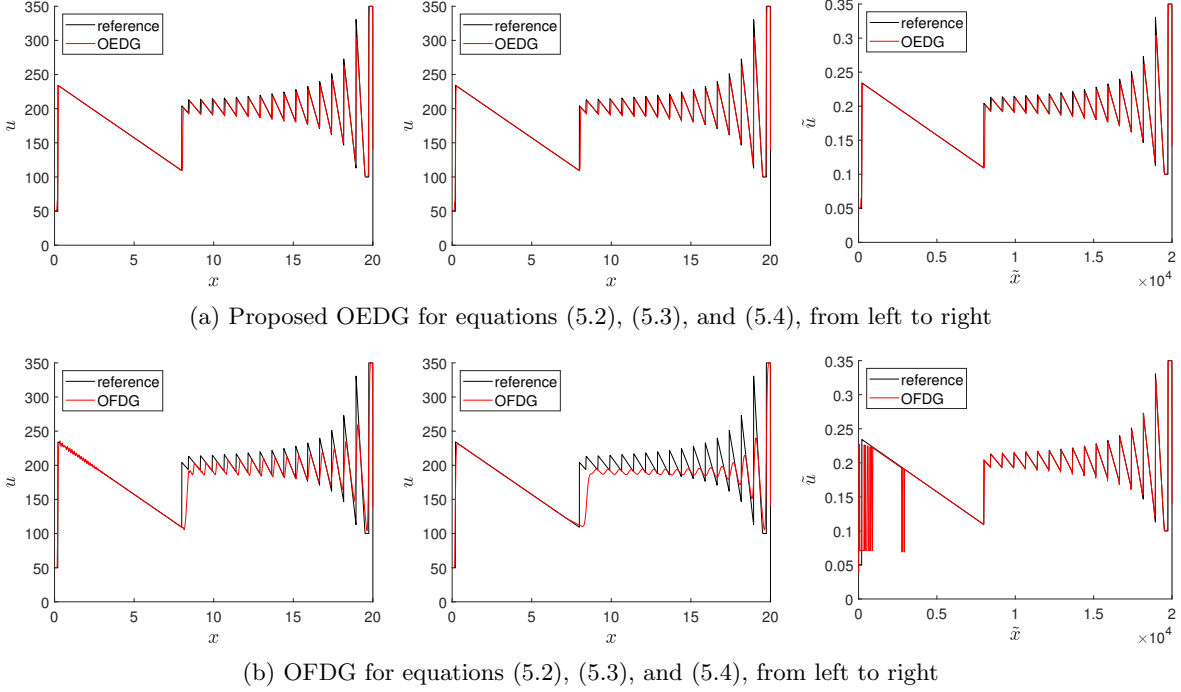


Fig. 2: Density at one hour computed by OEDG and OFDG methods solving three equivalent equations in different units for Example 5.4. Cell averages are plotted.

Example 5.5 (smooth problem). This example tests a smooth problem with the exact solution

$$\rho(x, t) = 2 + 2 \sin^2(x - t), \quad v(x, t) = 1, \quad p(x, t) = 2.$$

The computational domain is $\Omega = [0, 2\pi]$ with periodic boundary conditions. The simulations are conducted up to $t = 1.1$. Table 4 gives the numerical errors and corresponding convergence rates for \mathbb{P}^k -based OEDG method with $(k + 1)$ th-order explicit RK time discretization with $C_{\text{CFL}} = \frac{0.95}{2k+1}$. Again, we observe the optimal $(k + 1)$ th-order convergence order for the \mathbb{P}^k -based OEDG method, as expected.

Example 5.6 (Lax problem). In this test, we investigate a classical Riemann problem, the Lax problem, with the scaled initial data $\mathbf{u}^\lambda(x, 0) = \lambda \mathbf{u}_0(x)$, where $\mathbf{u}_0(x) = (\rho_0, \rho_0 v_0, E_0)^\top$ is defined by

$$(\rho_0, v_0, p_0) = \begin{cases} (0.445, 0.698, 3.528), & x < 0, \\ (0.5, 0, 0.571), & x > 0. \end{cases}$$

We choose the computational domain $\Omega = [-5, 5]$ and apply outflow boundary conditions. It is noteworthy that the exact solution conforms to $\frac{1}{\lambda} \mathbf{u}^\lambda(x, t) = \mathbf{u}^1(x, t)$ for all $\lambda > 0$. To assess the scale-invariant property, we choose three different λ within $\{1, 0.01, 100\}$. Figure 3 presents the numerical solutions at $t = 1.3$ obtained using the third-order OEDG and OFDG methods, respectively, both with 256 uniform cells. For clarity, we plot the OFDG solution polynomials and cell averages; we also zoom in some regions where spurious oscillations are produced. It is seen that the OEDG solution is scale-invariant and effectively captures the shock and contact discontinuity, devoid of noticeable spurious oscillations across all values of λ . Conversely, the OFDG method with non-scale-invariant damping (2.13) yields inconsistent numerical outputs across different λ values. Specifically, Figure 3b clearly shows that the OFDG solution exhibits excessive smearing for $\lambda = 100$ and presents spurious oscillations proximate to the shock and contact discontinuity when $\lambda = 0.01$. Some undershoots are also observed in the OFDG solution polynomials near the shock even in the case of $\lambda = 1$. We would

Table 4: Errors and convergence rates for \mathbb{P}^k -based OEDG method for 1D Euler equations.

k	N_x	L^1 error	rate	L^2 error	rate	L^∞ error	rate
1	256	8.72e-4	2.78	4.01e-4	2.77	3.29e-4	2.71
	512	1.43e-4	2.61	6.60e-5	2.61	5.33e-5	2.63
	1024	2.68e-5	2.41	1.33e-5	2.31	1.07e-5	2.32
	2048	5.86e-6	2.19	3.10e-6	2.11	3.03e-6	1.81
	4096	1.42e-6	2.05	7.58e-7	2.03	8.04e-7	1.91
	8192	3.50e-7	2.02	1.89e-7	2.01	2.07e-7	1.96
	16384	8.70e-8	2.01	4.71e-8	2.00	5.25e-8	1.98
2	256	5.12e-6	4.02	2.60e-6	3.93	2.39e-6	3.81
	512	4.84e-7	3.40	2.46e-7	3.40	2.25e-7	3.40
	1024	5.49e-8	3.14	2.78e-8	3.14	2.51e-8	3.17
	2048	6.63e-9	3.05	3.36e-9	3.05	3.00e-9	3.06
	4096	8.20e-10	3.01	4.15e-10	3.02	3.69e-10	3.03
3	256	1.40e-8	-	6.31e-9	-	4.45e-9	-
	512	4.51e-10	4.95	2.07e-10	4.93	1.60e-10	4.80
	1024	1.58e-11	4.83	7.59e-12	4.77	6.32e-12	4.66
	2048	7.57e-13	4.39	3.57e-13	4.41	4.11e-13	3.94

like to point out that the results of OFDG method will be improved if the scale-invariant damping (2.6) is employed to replace its original damping (2.13).

Example 5.7 (Woodward–Colella blast wave). This example simulates the interaction of two blast waves in the domain $[0, 1]$ with reflective boundary conditions. The initial conditions are defined as

$$(\rho_0, v_0, p_0) = \begin{cases} (1, 0, 10^3), & 0 < x < 0.1, \\ (1, 0, 10^{-2}), & 0.1 < x < 0.9, \\ (1, 0, 10^2), & 0.9 < x < 1. \end{cases}$$

Figure 4 displays the numerical results at $t = 0.038$ obtained by using the proposed OEDG method, in comparison with the OFDG method, both on the uniform mesh of 640 cells. Here the DG solution polynomials are plotted. The reference solution is computed by using the local Lax–Friedrichs scheme on a fine mesh of 100,000 uniform cells. For comparison, we also present the numerical solutions computed with or without characteristic decomposition. As seen from Figure 4, the OFDG method exhibits much smearing without using characteristic decomposition, which is necessitated to achieve satisfactory results—a finding that aligns with observations in [21, Figure 3.5]. In contrast, the proposed OEDG method works well either with or without the use of characteristic decomposition, and notably, it offers superior resolution compared to the OFDG method.

Example 5.8 (Shu–Osher problem). In this example, we consider the Shu–Osher problem, with the scaled initial data $\mathbf{u}^\lambda(x, 0) = \lambda \mathbf{u}_0(x)$, where $\mathbf{u}_0(x) = (\rho_0, \rho_0 v_0, E_0)^\top$ defined by

$$(\rho_0, v_0, p_0) = \begin{cases} (3.857143, 2.629369, 10.33333), & x < -4, \\ (1 + 0.2\sin(5x), 0, 1), & x > -4. \end{cases}$$

This problem describes the interaction of sine waves and a right-moving shock. It is typically used to examine the capability of high-order numerical schemes. We vary λ within $\{1, 0.01, 100\}$ to demonstrate the importance of ensuring scale invariance. Figure 5 reports the numerical results at $t = 1.8$ simulated by the OEDG and OFDG methods, respectively, both using the \mathbb{P}^3 DG element with 400 uniform cells. Here the DG solution polynomials are plotted. The reference solution is computed by using the local Lax–Friedrichs scheme on a very fine mesh of 300,000 uniform cells. We see that the proposed OEDG method exactly maintains the scale invariance and provides consistently good results without spurious oscillations for all λ . The OFDG method with non-scale-invariant damping (2.13),

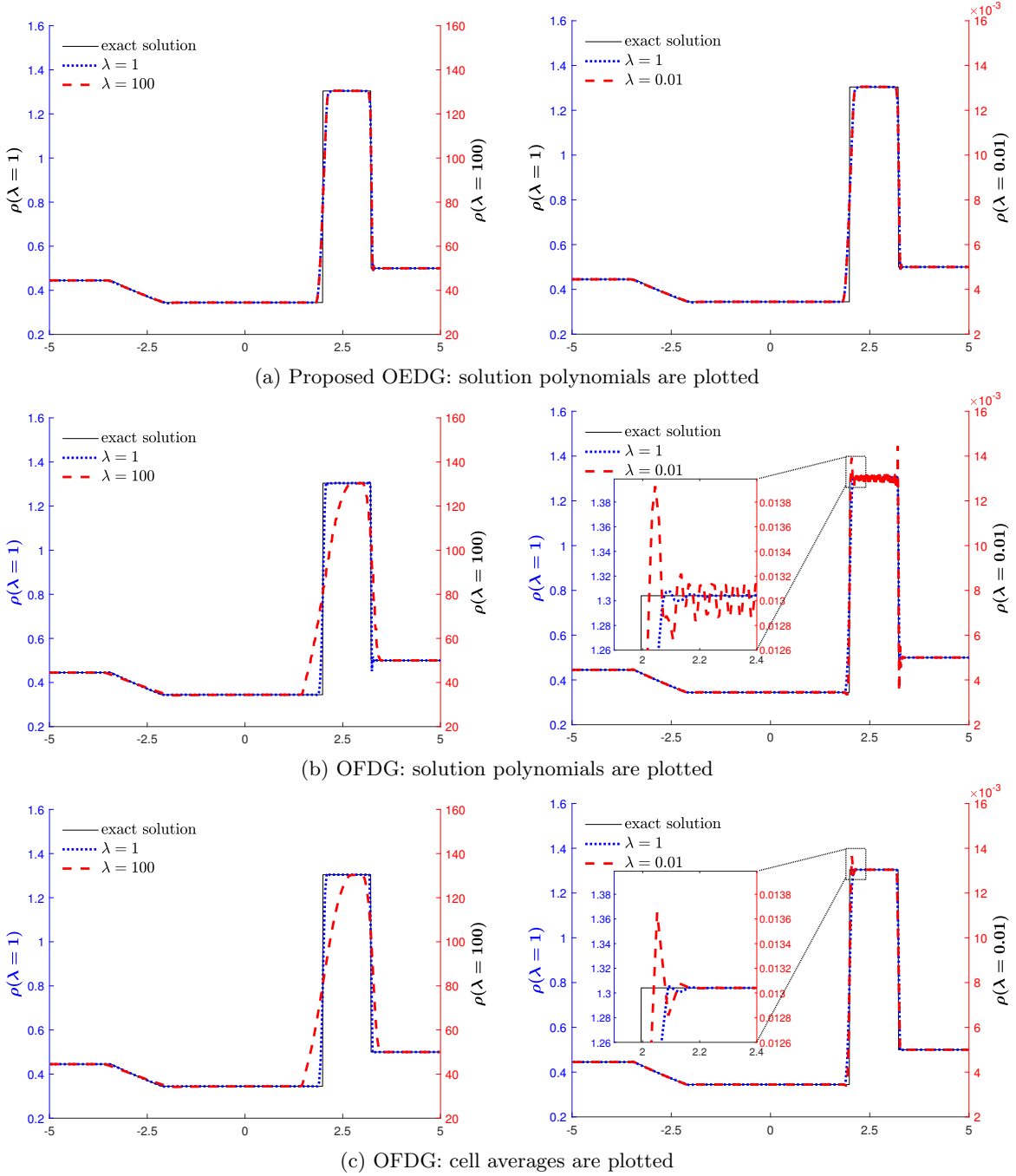


Fig. 3: Density of Lax problem at $t = 1.3$ computed by OEDG and OFDG methods.

although giving satisfactory solution for $\lambda = 1$, yields some small spurious oscillations when $\lambda = 0.01$ and produces too much dissipation in the case of $\lambda = 100$. This, again, underscores the importance of ensuring scale invariance when simulating problems across different scales.

5.5. 2D linear advection equation. In this subsection, we present two 2D examples of the advection equation $u_t + u_x + u_y = 0$ in the domain $\Omega = [-1, 1]^2$ with periodic boundary conditions.

Example 5.9 (smooth problem). The first example serves as a smooth test case to validate the

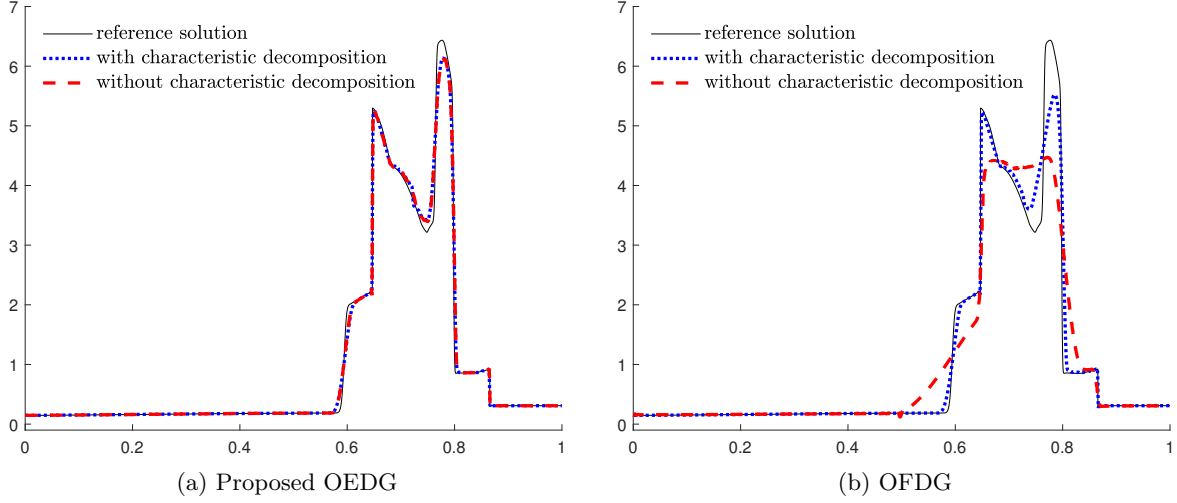


Fig. 4: Density of Woodward–Colella blast wave problem at $t = 0.038$ computed by OEDG and OFDG methods with or without characteristic decomposition. Solution polynomials are plotted.

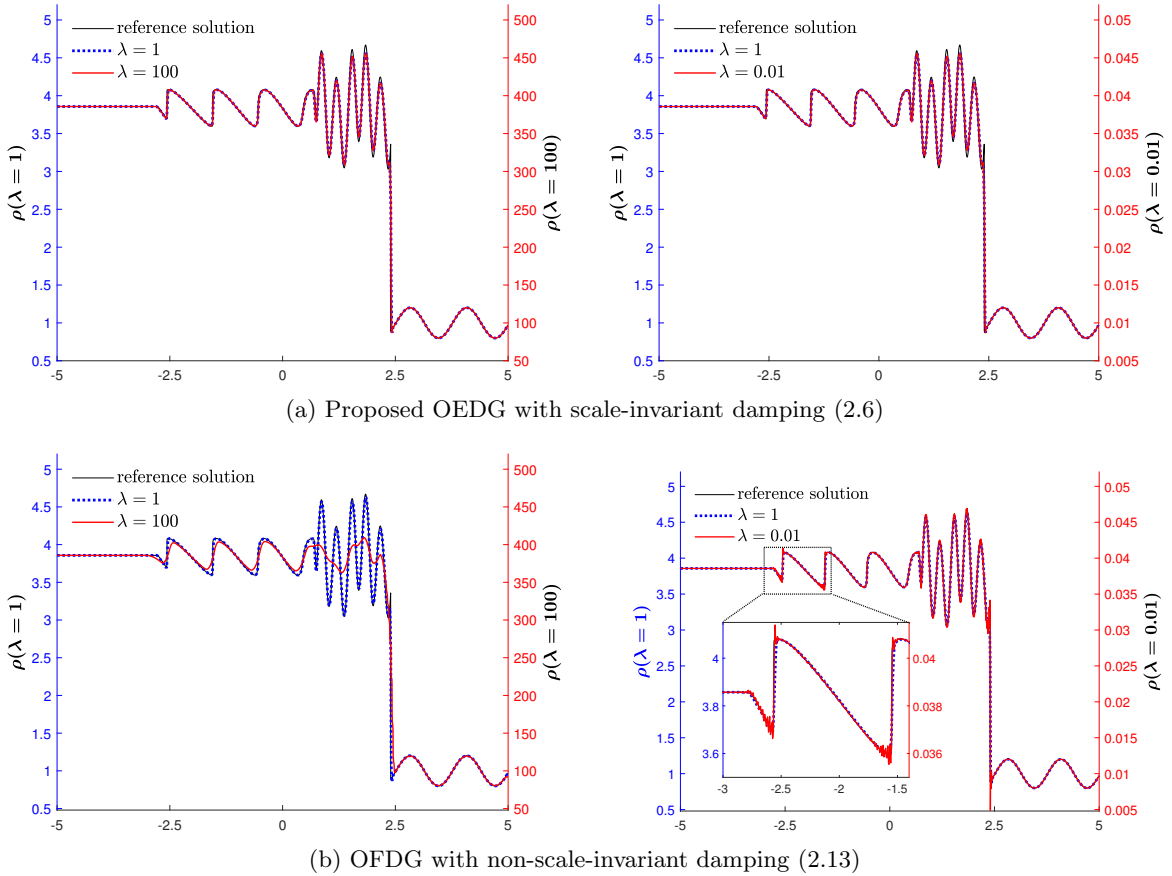


Fig. 5: Density of Shu–Osher problem at $t = 1.8$ computed by OEDG and OFDG methods. Solution polynomials are plotted.

accuracy of the proposed 2D OEDG schemes. The initial solution is $u_0(x, y) = \sin^2(\pi(x+y))$. Table 5 lists the numerical errors at $t = 1.1$ and corresponding convergence orders in three different norms

for the 2D \mathbb{P}^k -based OEDG method with $(k + 1)$ th-order RK time discretization. We observe that the convergence rates surpass the theoretical rate of $k + 1$. This is because the high-order damping effect dominates the errors on coarse meshes. However, as the mesh is refined, the convergence rates will progressively approach the anticipated theoretical rate. Similar phenomena were also observed for the 2D OFDG method in [24, Table 4.3].

Table 5: Errors and convergence rates for 2D \mathbb{P}^k -based OEDG method for Example 5.9.

k	$N_x \times N_y$	L^1 error	rate	L^2 error	rate	L^∞ error	rate
1	80×64	1.46e-2	-	1.80e-2	-	3.25e-2	-
	160×128	2.56e-3	2.51	2.95e-3	2.61	5.23e-3	2.64
	320×256	3.85e-4	2.74	4.45e-4	2.73	7.57e-4	2.79
	640×512	5.89e-5	2.71	7.07e-5	2.65	1.36e-4	2.48
	1280×1024	1.17e-5	2.33	1.35e-5	2.39	2.55e-5	2.41
	2560×2048	2.73e-6	2.10	3.06e-6	2.15	5.38e-6	2.25
2	80×64	2.15e-3	-	2.42e-3	-	3.95e-3	-
	160×128	8.69e-5	4.63	9.63e-5	4.65	1.53e-4	4.69
	320×256	5.48e-6	3.99	6.09e-6	3.98	1.05e-5	3.87
	640×512	3.53e-7	3.96	3.94e-7	3.95	7.80e-7	3.75
	1280×1024	2.37e-8	3.90	2.70e-8	3.87	6.49e-8	3.59
	2560×2048	1.76e-9	3.75	2.10e-9	3.68	6.24e-9	3.38
3	80×64	1.90e-4	6.11	2.22e-4	6.00	3.91e-4	5.79
	160×128	4.99e-6	5.25	5.78e-6	5.27	1.02e-5	5.26
	320×256	1.60e-7	4.96	1.87e-7	4.95	3.83e-7	4.74
	640×512	5.22e-9	4.94	6.25e-9	4.91	1.56e-8	4.62
	1280×1024	1.84e-10	4.83	2.36e-10	4.73	7.65e-10	4.35

Example 5.10 (pentagram discontinuities). The initial solution of this example is discontinuous:

$$u_0(x, y) = \begin{cases} 1, & r \leq \frac{1}{8}(3 + 3^{\sin(5\theta)}), \\ 0, & \text{otherwise,} \end{cases} \quad \theta = \begin{cases} \arccos(\frac{x}{r}), & y \geq 0, \\ 2\pi - \arccos(\frac{x}{r}), & y < 0, \end{cases}$$

where $r = \sqrt{x^2 + y^2}$. The computational domain $\Omega = [-1, 1]^2$ is divided into 320×320 uniform rectangular cells. The DG solutions at $t = 1.8$ obtained by using the OEDG schemes are visualized in Figure 6. We see that the numerical solutions agree well with the exact one, and the discontinuities in a pentagram shape are correctly captured with high resolution and without spurious oscillations.

5.6. 2D inviscid Burgers' equation. In this subsection, we consider the 2D Burgers' equation $u_t + (\frac{u^2}{2})_x + (\frac{u^2}{2})_y = 0$ in the domain $\Omega = [0, 1]^2$.

Example 5.11 (2D Riemann problem). This is a 2D Riemann problem with the initial data given by

$$u_0(x, y) = \begin{cases} 0.5, & x < 0.5, y < 0.5, \\ 0.8, & x > 0.5, y < 0.5, \\ -1, & x > 0.5, y > 0.5, \\ -0.2, & x < 0.5, y > 0.5. \end{cases}$$

The computational domain Ω is partitioned into 256×256 uniform rectangular cells. Outflow boundary conditions are imposed on all the edges of Ω . Figure 7 presents the DG solutions at $t = 0.5$ computed using the OEDG schemes with \mathbb{P}^1 , \mathbb{P}^2 , and \mathbb{P}^3 elements, respectively. It is worth noting that the numerical solutions exhibit no spurious oscillations.

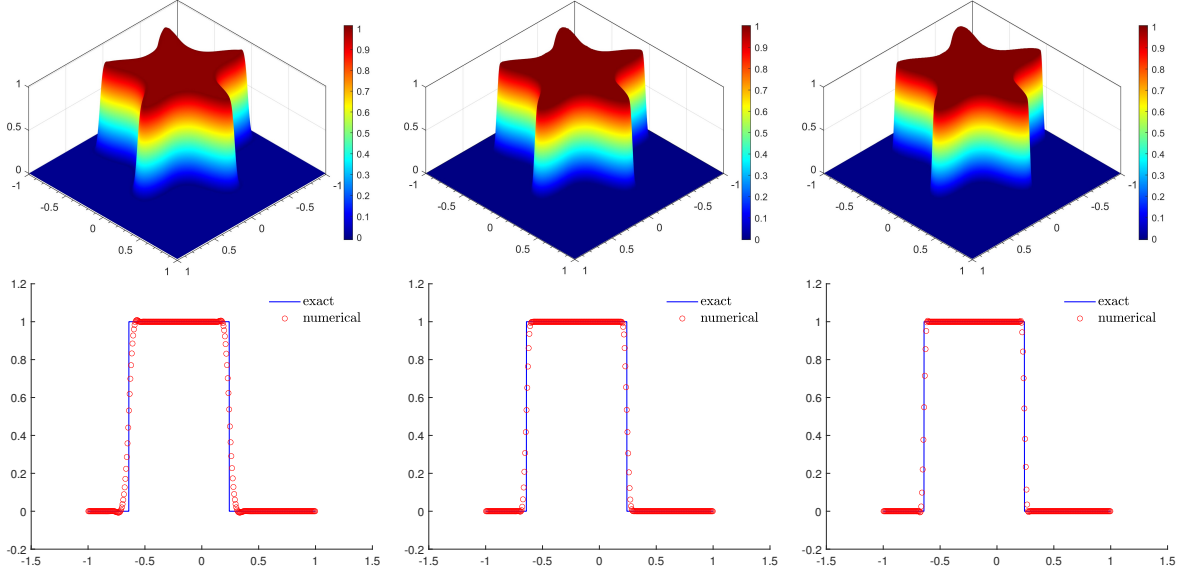


Fig. 6: OEDG solutions (top) at $t = 1.8$ and their cut along $y = -0.25$ (bottom) for Example 5.10. From left to right: \mathbb{P}^1 , \mathbb{P}^2 , and \mathbb{P}^3 elements.

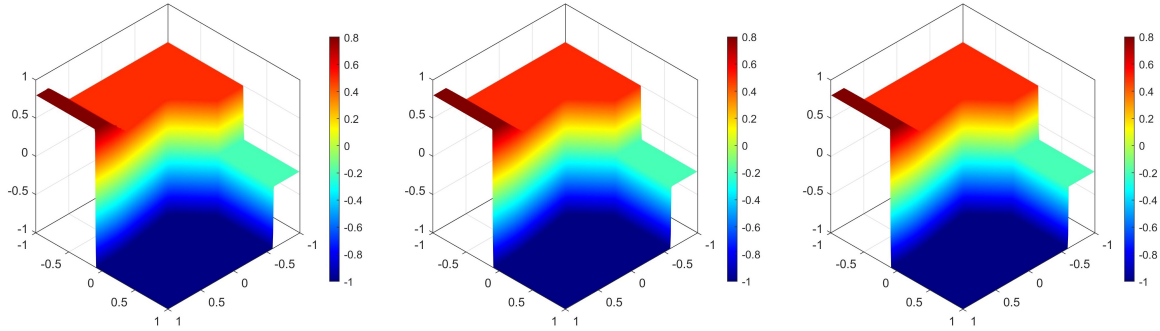


Fig. 7: OEDG solutions at $t = 0.5$ for Example 5.11. From left to right: \mathbb{P}^1 , \mathbb{P}^2 , and \mathbb{P}^3 elements.

5.7. 2D compressible Euler equations. This subsection presents several benchmark numerical tests for the 2D compressible Euler equations. These equations can be expressed in the form of (3.1) with $\mathbf{u} = (\rho, \rho\mathbf{v}, E)^\top$ and $\mathbf{f}(\mathbf{u}) = (\rho\mathbf{v}, \rho\mathbf{v} \otimes \mathbf{v} + p\mathbf{I}, (E + p)\mathbf{v})^\top$. Here ρ represents the density, \mathbf{v} denotes the velocity field, and p is the pressure. The total energy is given by $E = \frac{1}{2}\rho|\mathbf{v}|^2 + \frac{p}{\gamma-1}$, and the adiabatic index γ is set to 1.4 unless specified otherwise.

Example 5.12 (smooth problem). The exact solution of this problem is given by

$$(\rho, \mathbf{v}, p) = (1 + 0.2 \sin(\pi(x + y - t)), 0.7, 0.3, 1),$$

which describes a sine wave that propagates periodically within the domain $[0, 2]^2$. Table 6 shows the numerical errors and corresponding convergence orders for the density at $t = 2$ obtained by the 2D \mathbb{P}^k -based OEDG method with $(k + 1)$ th-order RK time discretization. One can observe that the convergence orders are above the theoretical order of $k + 1$, incrementally nearing $k + 1$ as the mesh is refined.

Example 5.13 (shock reflection problem). In this example, we simulate the shock reflection problem (cf. [42]) in the domain $\Omega = [0, 4] \times [0, 1]$. The initial conditions are defined as $(\rho_0, \mathbf{v}_0, p_0) = (1, 2.9, 0, \frac{5}{7})$, which are also imposed as inflow condition on the left boundary of Ω . The upper bound-

Table 6: Errors and convergence rates for 2D \mathbb{P}^k -based OEDG method for Example 5.12.

	$N_x \times N_y$	L^1 error	rate	L^2 error	rate	L^∞ error	rate
1	80×80	1.83e-4	-	2.08e-4	-	4.39e-4	-
	160×160	2.52e-5	2.86	2.94e-5	2.82	6.81e-5	2.69
	320×320	3.85e-6	2.71	4.60e-6	2.68	1.17e-5	2.54
	640×640	7.08e-7	2.44	8.83e-7	2.38	2.27e-6	2.37
	1280×1280	1.53e-7	2.21	2.00e-7	2.14	4.85e-7	2.23
2	80×80	6.10e-4	-	7.85e-4	-	1.54e-3	-
	160×160	3.82e-6	7.32	4.37e-6	7.49	7.94e-6	7.60
	320×320	1.56e-7	4.61	1.77e-7	4.63	3.36e-7	4.56
	640×640	9.14e-9	4.09	1.06e-8	4.06	2.36e-8	3.83
	1280×1280	6.13e-10	3.90	7.57e-10	3.81	2.00e-9	3.56
3	80×80	7.66e-7	-	1.01e-6	-	2.86e-6	-
	160×160	1.35e-8	5.83	1.57e-8	6.01	3.32e-8	6.43
	320×320	3.98e-10	5.08	4.50e-10	5.12	8.73e-10	5.25
	640×640	1.25e-11	4.99	1.42e-11	4.99	3.26e-11	4.74

ary is also specified as inflow condition but with a different state

$$(\rho, \mathbf{v}, p) = (1.69997, 2.61934, -0.50632, 1.52819).$$

The reflective wall boundary condition is applied to the lower boundary, while the outflow boundary condition is used on the right boundary. The density contour plot at $t = 20$, computed using the third-order OEDG scheme on a uniform rectangular mesh of 200×50 cells, are presented in Figure 8a. As time evolves, the solution converges to a steady state. To study the convergence behavior, we follow [42, 21] and compute the average residue as

$$(5.5) \quad \text{Res} := \frac{1}{4N_x N_y} \sum_{i=1}^{N_x} \sum_{j=1}^{N_y} \sum_{q=1}^4 |R_{ij}^{(q)}|,$$

where $R_{ij}^{(q)} := \frac{1}{\tau}(u_h^{n+1,(q)} - u_h^{n,(q)})$ denotes the local residue on the cell $[x_{i-\frac{1}{2}}, x_{i+\frac{1}{2}}] \times [y_{j-\frac{1}{2}}, y_{j+\frac{1}{2}}]$ for the q th component of the conservative vector \mathbf{u}_h . The convergence history of the average residue over time is plotted Figure 8b. It is seen that the average residue reaches tiny values close to the machine epsilon in double precision and remains at that level after about $t = 9$.

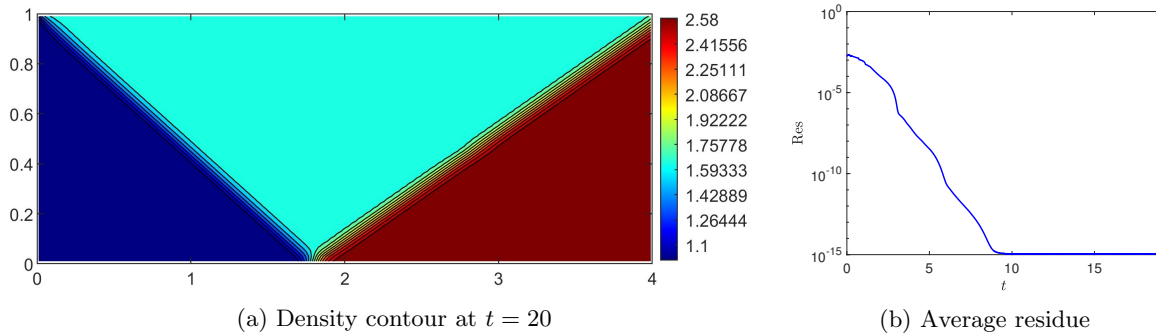


Fig. 8: Shock reflection problem simulated by third-order OEDG scheme.

Example 5.14 (supersonic flow past two plates). This example simulates a supersonic flow past two plates, with an attack angle of 15° , in the domain $[0, 10] \times [-5, 5]$ as detailed in [42]. The initial

condition is given by

$$(\rho_0, \mathbf{v}_0, p_0) = \left(1, \cos\left(\frac{\pi}{12}\right), \sin\left(\frac{\pi}{12}\right), \frac{1}{\gamma M_\infty^2} \right),$$

where $M_\infty = 3$ represents the Mach number of the free stream. The plates are situated at $y = \pm 2$ with $x \in (2, 3)$, where slip boundary conditions are imposed. The inflow boundary conditions are set on the left and lower boundaries, whereas the outflow conditions are specified on the upper and right boundaries. The simulation is conducted until $t = 100$ using the third-order OEDG scheme on a mesh of 200×200 uniform cells. The results are illustrated in Figure 9a, showing the numerical solution at the steady state at $t = 100$. We see that the flow structures are correctly captured by the OEDG method without nonphysical oscillations. Figure 9b presents the convergence history of the average residue over time, which is computed by (5.5). It is observed that the average residue settles down to tiny values around the machine epsilon in double precision.

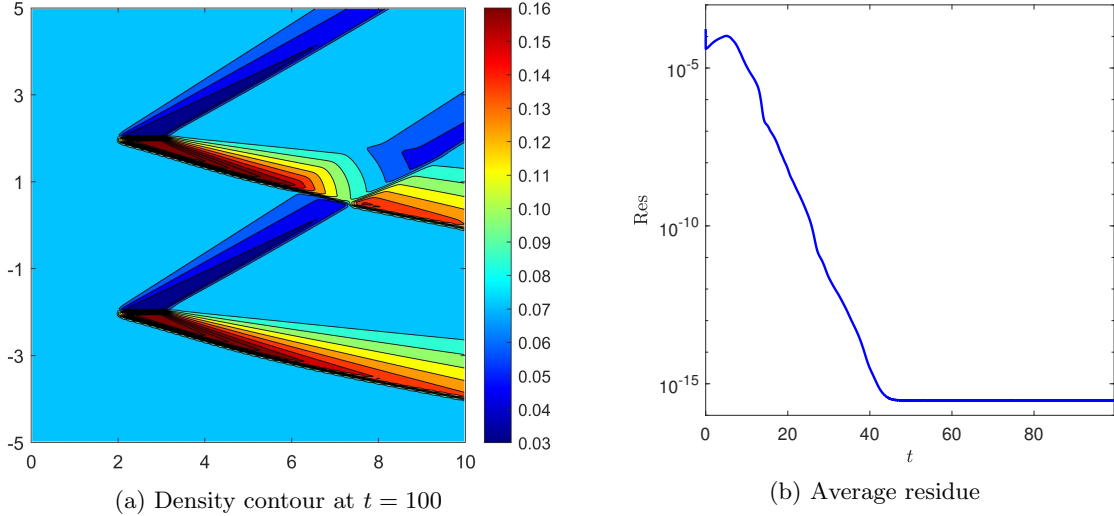


Fig. 9: Supersonic flow problem simulated by third-order OEDG scheme.

Example 5.15 (2D Riemann problems). In this example, we investigate two classic 2D Riemann problems of the Euler equations in the domain $[0, 1] \times [0, 1]$ with outflow boundary conditions. To check the scale-invariant property of the 2D OEDG method, we consider the scaled initial data $\mathbf{u}^\lambda(x, 0) = \lambda \mathbf{u}_0(x)$, where the scaling represents the use of different units for \mathbf{u} . For the first Riemann problem, $\mathbf{u}_0(x)$ is given by

$$(\rho_0, \mathbf{v}_0, p_0) = \begin{cases} (0.8, 0, 0, 1), & x < 0.5, y < 0.5, \\ (1, 0.7276, 0, 1), & x < 0.5, y > 0.5, \\ (1, 0, 0.7276, 1), & x > 0.5, y < 0.5, \\ (0.5313, 0, 0, 0.4), & x > 0.5, y > 0.5, \end{cases}$$

which involve two stationary contact discontinuities and two shocks. The initial solution $\mathbf{u}_0(x)$ of the second Riemann problem is defined by

$$(\rho_0, \mathbf{v}_0, p_0) = \begin{cases} (0.138, 1.206, 1.206, 0.029), & x < 0.5, y < 0.5, \\ (0.5323, 1.206, 0, 0.3), & x < 0.5, y > 0.5, \\ (0.5323, 0, 1.206, 0.3), & x > 0.5, y < 0.5, \\ (1.5, 0, 0, 1.5), & x > 0.5, y > 0.5. \end{cases}$$

Figure 10 presents the numerical results of the first Riemann problem simulated by the third-order OEDG and OFDG methods, respectively, on the rectangular mesh of 320×320 uniform cells for

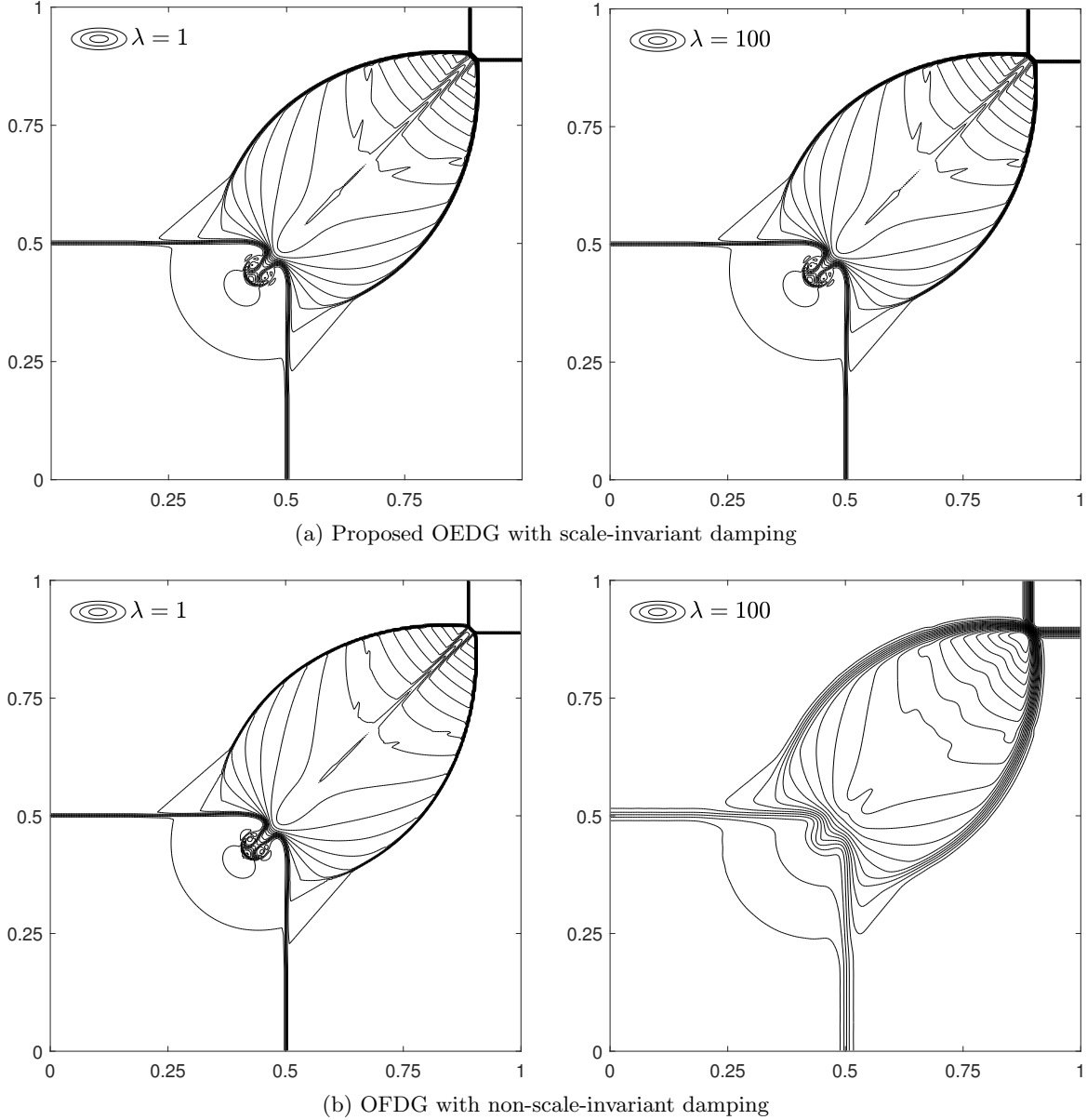


Fig. 10: Contour plots of density at $t = 0.25$ computed by OEDG and OFDG methods.

two distinct cases ($\lambda = 1$ and $\lambda = 100$). The results for the second Riemann problem are depicted in Figure 11. For the normal scale with $\lambda = 1$, both OEDG and OFDG methods yield satisfactory results, capturing the solution accurately without producing excessive dissipation or nonphysical oscillations. Yet, when $\lambda = 100$, the damping terms in the OFDG method escalate to λ^2 times its original magnitudes, causing excessive smearing and smoothing out the detailed features near discontinuities. Contrarily, the OEDG method consistently produces satisfactory results agreeing with those in the normal scale case, thanks to its scale-invariant advantage. It is worth mentioning that the results of OFDG method will be improved if our scale-invariant damping (3.9) is employed.

Example 5.16 (shock-vortex interaction). Consider the interaction between a vortex and a Mach 1.1 shock, which is perpendicular to the x -axis and located at $x = 0.5$. The left state of the shock is $(\rho, \mathbf{v}, p) = (1, 1.1\sqrt{\gamma}, 0, 1)$, while the right state is derived from the Rankine–Hugoniot condition. Initially, an isentropic vortex, centered at $(x_c, y_c) = (0.25, 0.5)$, is superimposed on the mean flow

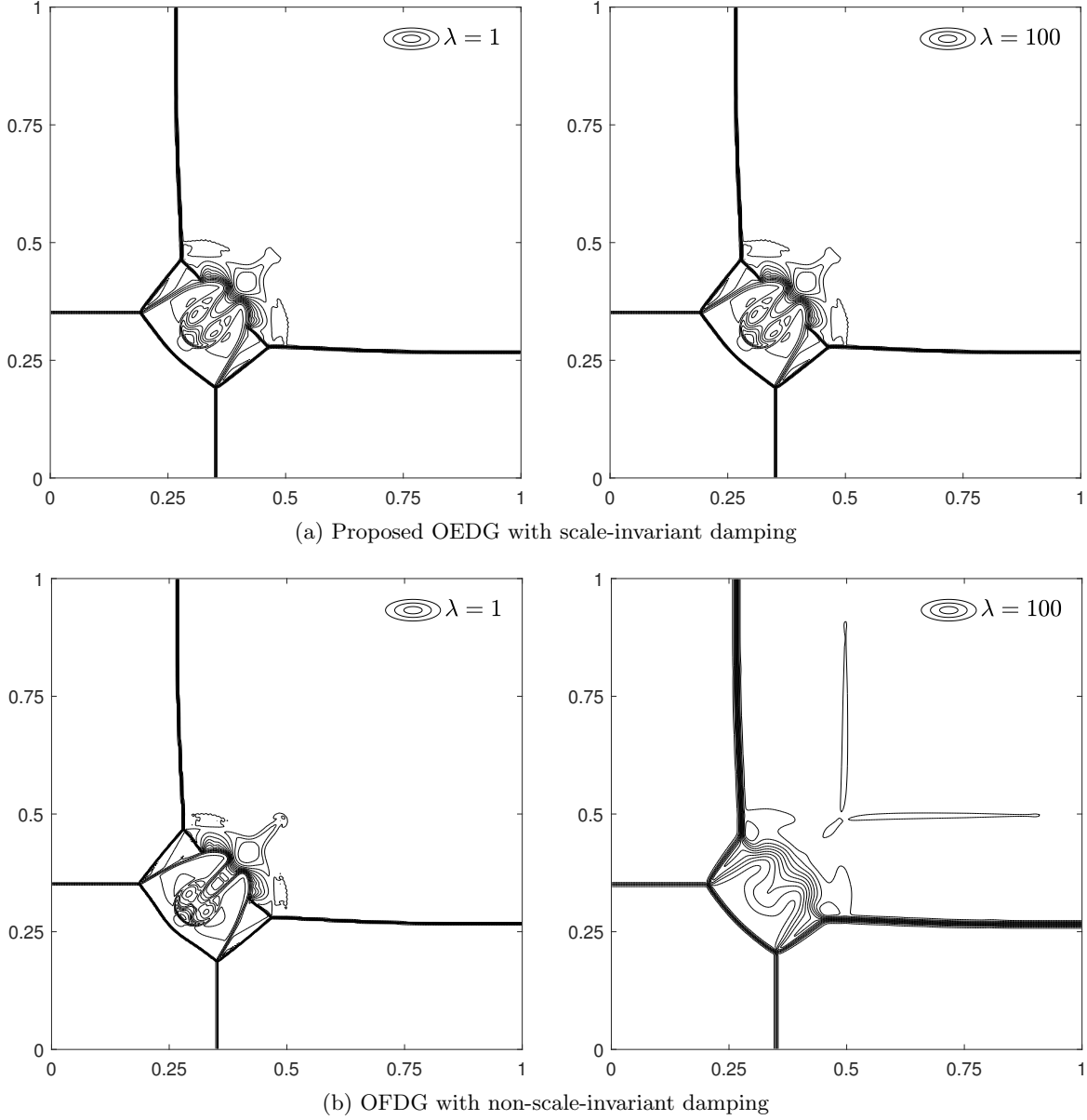


Fig. 11: Contour plots of density at $t = 0.35$ computed by OEDG and OFDG methods.

to the left of the shock. The velocity, temperature, and entropy perturbations due to the vortex are defined by

$$\delta \mathbf{v} = \frac{\varepsilon}{r_c} e^{\alpha(1-\eta^2)} (\bar{y}, -\bar{x}), \quad \delta T = -\frac{(\gamma-1)\varepsilon^2}{4\alpha\gamma} e^{2\alpha(1-\eta^2)}, \quad \delta S = 0,$$

where $r^2 = \bar{x}^2 + \bar{y}^2$, $\eta = \frac{r}{r_c}$, and $(\bar{x}, \bar{y}) = (x - x_c, y - y_c)$. The parameters $\varepsilon = 0.3$, $\alpha = 0.204$, and $r_c = 0.05$ represent the vortex's strength, decay rate, and critical radius, respectively. The computational domain is set as $[0, 2] \times [0, 1]$ and is divided into 400×200 uniform rectangular cells. Reflective boundary conditions are applied on both the upper and lower boundaries, while the left and right boundaries utilize inflow and outflow conditions, respectively. The third-order OEDG method is employed for simulations up to $t = 0.8$. Contour plots of pressure at six distinct times are illustrated in Figure 12. These results are in good agreement with those reported in [21]. The OEDG

method effectively captures the shock-vortex interaction dynamics and accurately depicts intricate wave structures. Notably, the OEDG solution exhibits no nonphysical oscillations.

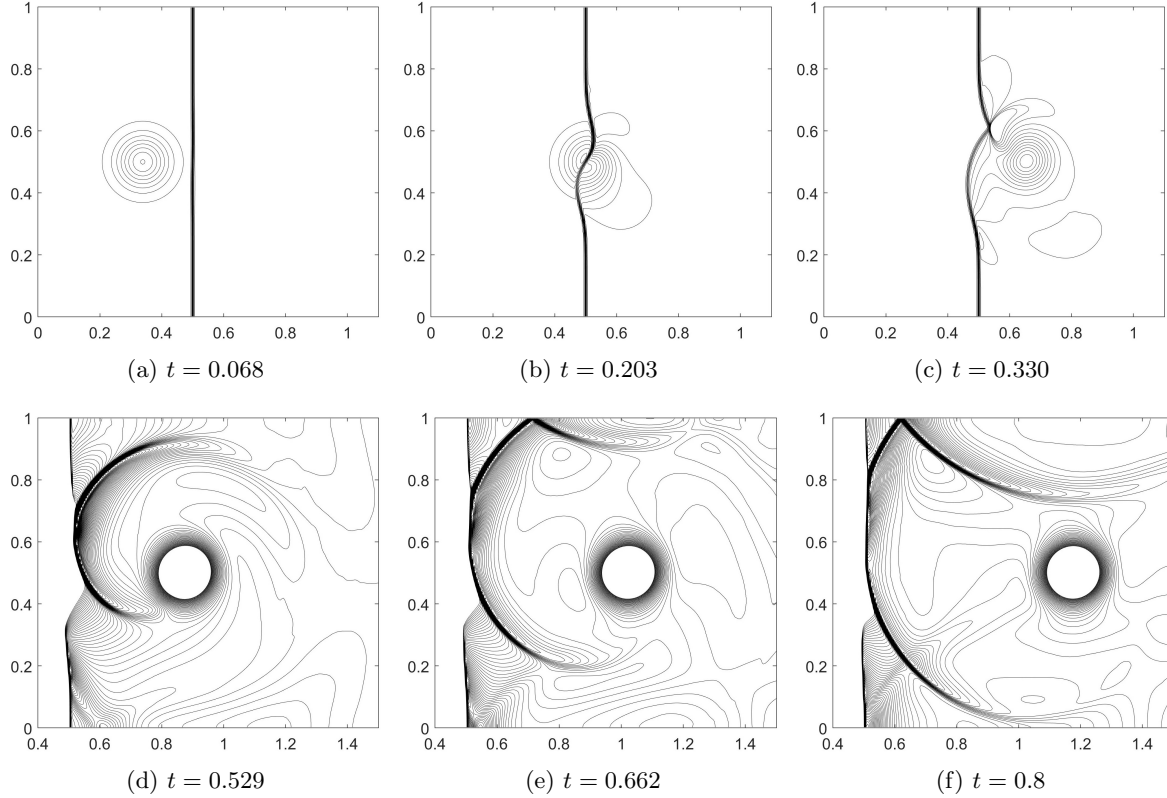


Fig. 12: Contour plots of pressure for shock-vortex interaction: 30 contour lines from 0.68 to 1.3 are shown in the top figures, while 90 contour lines from 1.19 to 1.36 are plotted in the bottom figures.

Example 5.17 (double Mach reflection). This is a classic test case in computational fluid dynamics for assessing the capabilities of numerical schemes in handling strong shocks and their interactions. The computational domain is a rectangular region $\Omega = [0, 4] \times [0, 1]$. Initially, an oblique shock with a Mach number of 10 propagates to the right. This shock originates at $(x, y) = (1/6, 0)$ and forms an angle of 60° relative to the bottom boundary. The states to the left and right of this shock are

$$(\rho_0, u_0, v_0, p_0) = \begin{cases} (8, 8.25 \cos(\frac{\pi}{6}), -8.25 \sin(\frac{\pi}{6}), 116.5), & x < \frac{1}{6} + \frac{y}{\sqrt{3}}, \\ (1.4, 0, 0, 1), & x > \frac{1}{6} + \frac{y}{\sqrt{3}}. \end{cases}$$

The left and right boundaries enforce inflow and outflow conditions, respectively. For the upper boundary, the postshock state is specified in the segment $x = 0$ to $x = \frac{1}{6} + \frac{1}{\sqrt{3}}(1 + 20t)$, while the preshock state is maintained for the remaining portion. On the lower boundary, the segment from $x = 0$ to $x = 1/6$ holds the postshock state, and a reflective boundary condition is applied to the remainder. We employ the proposed \mathbb{P}^3 -based OEDG method for the simulation on the uniform rectangular mesh with $h_x = h_y = 1/240$. The resulting density contour plot at $t = 0.2$ is visualized in Figure 13. The intricate flow characteristics, including the double Mach region, are finely delineated, with no nonphysical oscillations near the discontinuities observed.

Example 5.18 (Mach 2000 jet). In the last example, we further examine the robustness of the OEDG method through simulating a challenging jet problem [40, 21]. The ratio of heat capacity is set to be $\gamma = \frac{5}{3}$. The domain $\Omega = [0, 1] \times [-0.25, 0.25]$ is initially populated with a stationary fluid characterized by the state $(\rho, \mathbf{v}, p) = (0.5, 0, 0, 0.4127)$. A high-speed jet state $(\rho, \mathbf{v}, p) = (5, 800, 0, 0.4127)$

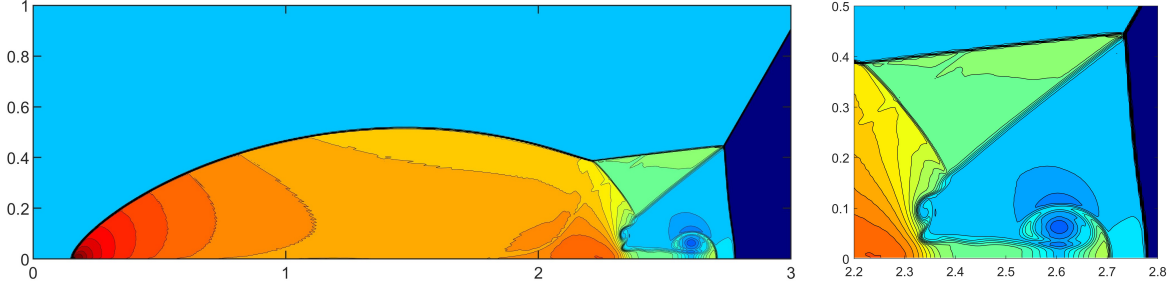


Fig. 13: The contour plot of density (left) and its close-up (right) at $t = 0.2$ obtained by the \mathbb{P}^3 -based OEDG method with $h_x = h_y = 1/240$.

is injected into Ω from the left boundary within the range $y = -0.05$ to 0.05 . Outflow conditions are applied to all remaining boundaries. Figure 14 presents the numerical results at $t = 0.001$ obtained by the third-order OEDG method with 320×160 cells. The intricate structures of the jet flow, including the bow shock and shear layer, are captured with high resolution and agree with those computed in [40, 21]. The OEDG method exhibits good robustness in this demanding test, and the computed solutions are free of nonphysical oscillations.

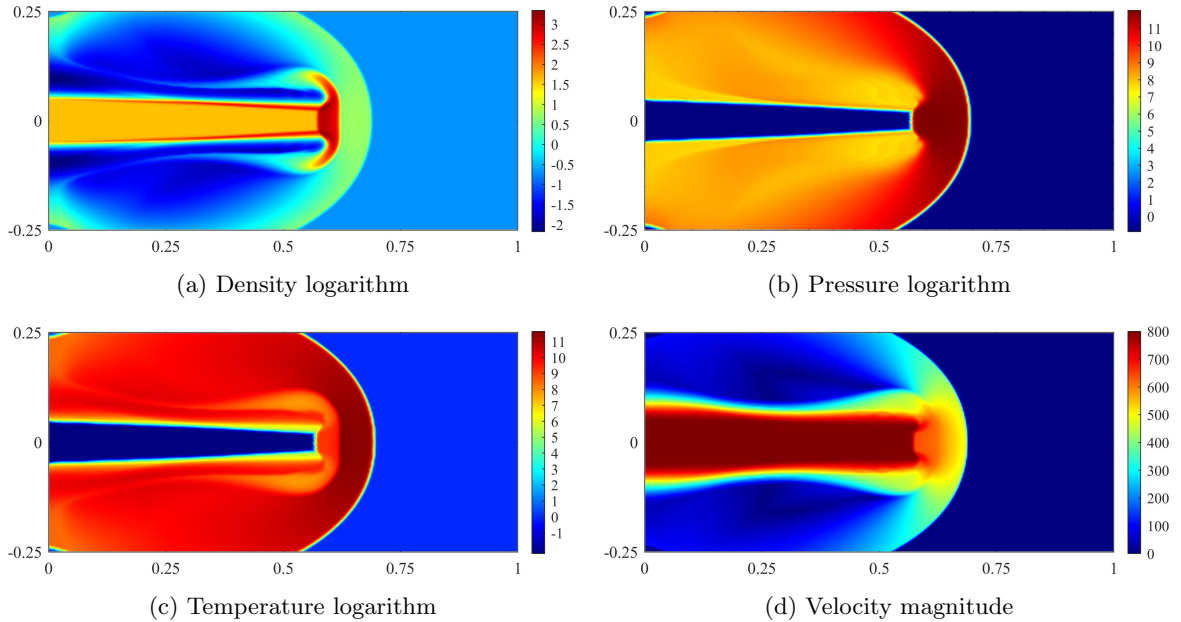


Fig. 14: Numerical results at $t = 0.001$ for the Mach 2000 jet problem.

6. Conclusions. This paper has proposed the oscillation-eliminating discontinuous Galerkin (OEDG) method, a novel, robust, and efficient numerical approach for hyperbolic conservation laws. This method is inspired by the damping technique of Lu, Liu, and Shu [24, 21]. The core principle behind the OEDG approach involves an alternate progression between the conventional DG scheme and a new damping equation. This leads to an OE procedure effectively eliminating spurious oscillations subsequent to each Runge–Kutta stage. The new damping equation possesses both scale-invariant and evolution-invariant properties, pivotal in ensuring oscillation-free DG solutions across diverse scales and wave speeds. With the exact solver for the damping equation, the OE procedure’s implementation becomes notably efficient, involving only simple multiplications of modal coefficients by scalars. One significant contribution of our work is the rigorous optimal error estimates for the fully discrete

OEDG method when applied to linear scalar conservation laws. To our knowledge, this might be the first effort on fully-discrete error estimates for nonlinear DG methods with an automatic oscillation control mechanism. Furthermore, the OEDG method has provided fresh perspectives on the damping technique for oscillation control. It has revealed the role of the damping operator as a modal filter and bridges the damping and spectral viscosity techniques.

The OEDG method offers several remarkable features. With its notable capacity to eliminate undesirable oscillations without necessitating problem-specific parameters, the OEDG method also eliminates the need for characteristic decomposition in hyperbolic systems. Furthermore, it retains many essential attributes of the conventional DG approach, such as conservation, optimal convergence rates, and superconvergence. Notably, even when confronted with strong shocks that lead to highly stiff damping terms, the OEDG method remains stable under the normal CFL condition. Another benefit of the OE procedure is its non-intrusive nature, allowing for easy integration into existing DG codes as an independent module. Our extensive numerical experiments have validated these theoretical findings, underscoring the effectiveness and superiority of the OEDG method on Cartesian meshes. The numerical tests on unstructured meshes will be reported in a separate paper.

It should be emphasized that the scale-invariant damping coefficients presented in (2.6) are not the sole choice. Indeed, they can be appropriately adjusted to preserve other important structures. As pointed out in Remark 2.9, the exploration of locally scale-invariant OEDG schemes would be of significant interest. We intend to pursue these investigations in our subsequent research efforts.

REFERENCES

- [1] J. AI, Y. XU, C.-W. SHU, AND Q. ZHANG, *L^2 error estimate to smooth solutions of high order Runge–Kutta discontinuous Galerkin method for scalar nonlinear conservation laws with and without sonic points*, SIAM Journal on Numerical Analysis, 60 (2022), pp. 1741–1773.
- [2] R. BECKER AND M. BRAACK, *A two-level stabilization scheme for the Navier-Stokes equations*, in Numerical Mathematics and Advanced Applications: Proceedings of ENUMATH 2003 the 5th European Conference on Numerical Mathematics and Advanced Applications Prague, August 2003, Springer, 2004, pp. 123–130.
- [3] M. BRAACK AND E. BURMAN, *Local projection stabilization for the Oseen problem and its interpretation as a variational multiscale method*, SIAM Journal on Numerical Analysis, 43 (2006), pp. 2544–2566.
- [4] Y. CHEN AND K. WU, *A physical-constraint-preserving finite volume WENO method for special relativistic hydrodynamics on unstructured meshes*, Journal of Computational Physics, 466 (2022), p. 111398.
- [5] Y. CHENG, X. MENG, AND Q. ZHANG, *Application of generalized Gauss–Radau projections for the local discontinuous Galerkin method for linear convection-diffusion equations*, Mathematics of Computation, 86 (2017), pp. 1233–1267.
- [6] B. COCKBURN, S. HOU, AND C.-W. SHU, *The Runge–Kutta local projection discontinuous Galerkin finite element method for conservation laws. IV. the multidimensional case*, Mathematics of Computation, 54 (1990), pp. 545–581.
- [7] B. COCKBURN, S.-Y. LIN, AND C.-W. SHU, *TVB Runge–Kutta local projection discontinuous Galerkin finite element method for conservation laws III: one-dimensional systems*, Journal of Computational Physics, 84 (1989), pp. 90–113.
- [8] B. COCKBURN AND C.-W. SHU, *TVB Runge–Kutta local projection discontinuous Galerkin finite element method for conservation laws. II. general framework*, Mathematics of computation, 52 (1989), pp. 411–435.
- [9] B. COCKBURN AND C.-W. SHU, *The Runge–Kutta local projection P^1 -discontinuous-Galerkin finite element method for scalar conservation laws*, ESAIM: Mathematical Modelling and Numerical Analysis, 25 (1991), pp. 337–361.
- [10] B. COCKBURN AND C.-W. SHU, *The Runge–Kutta discontinuous Galerkin method for conservation laws V: multidimensional systems*, Journal of Computational Physics, 141 (1998), pp. 199–224.
- [11] V. DOLEJŠÍ, M. FEISTAUER, AND C. SCHWAB, *A finite volume discontinuous Galerkin scheme for nonlinear convection-diffusion problems*, Calcolo, 39 (2002), pp. 1–40.
- [12] W. S. DON, R. LI, B.-S. WANG, AND Y. WANG, *A novel and robust scale-invariant WENO scheme for hyperbolic conservation laws*, Journal of Computational Physics, 448 (2022), p. 110724.
- [13] J. DU, Y. LIU, AND Y. YANG, *An oscillation-free bound-preserving discontinuous Galerkin method for multi-component chemically reacting flows*, Journal of Scientific Computing, 95 (2023), p. 90.
- [14] D. GOTTLIEB AND J. S. HESTHAVEN, *Spectral methods for hyperbolic problems*, Journal of Computational and Applied Mathematics, 128 (2001), pp. 83–131.
- [15] J. HESTHAVEN AND R. KIRBY, *Filtering in Legendre spectral methods*, Mathematics of Computation, 77 (2008), pp. 1425–1452.
- [16] J. S. HESTHAVEN, S. GOTTLIEB, AND D. GOTTLIEB, *Spectral methods for time-dependent problems*, vol. 21, Cambridge University Press, 2007.
- [17] A. HILTEBRAND AND S. MISHRA, *Entropy stable shock capturing space-time discontinuous Galerkin schemes for*

- systems of conservation laws*, Numerische Mathematik, 126 (2014), pp. 103–151.
- [18] J. HUANG AND Y. CHENG, *An adaptive multiresolution discontinuous Galerkin method with artificial viscosity for scalar hyperbolic conservation laws in multidimensions*, SIAM Journal on Scientific Computing, 42 (2020), pp. A2943–A2973.
- [19] J. HUANG AND C.-W. SHU, *Error estimates to smooth solutions of semi-discrete discontinuous Galerkin methods with quadrature rules for scalar conservation laws*, Numerical Methods for Partial Differential Equations, 33 (2017), pp. 467–488.
- [20] J. HUANG AND C.-W. SHU, *Bound-preserving modified exponential Runge–Kutta discontinuous Galerkin methods for scalar hyperbolic equations with stiff source terms*, Journal of Computational Physics, 361 (2018), pp. 111–135.
- [21] Y. LIU, J. LU, AND C.-W. SHU, *An essentially oscillation-free discontinuous Galerkin method for hyperbolic systems*, SIAM Journal on Scientific Computing, 44 (2022), pp. A230–A259.
- [22] Y. LIU, J. LU, Q. TAO, AND Y. XIA, *An oscillation-free discontinuous Galerkin method for shallow water equations*, Journal of Scientific Computing, 92 (2022), p. 109.
- [23] Y. LIU, C.-W. SHU, AND M. ZHANG, *Optimal error estimates of the semidiscrete discontinuous Galerkin methods for two dimensional hyperbolic equations on Cartesian meshes using P^k elements*, ESAIM: Mathematical Modelling and Numerical Analysis, 54 (2020), pp. 705–726.
- [24] J. LU, Y. LIU, AND C.-W. SHU, *An oscillation-free discontinuous Galerkin method for scalar hyperbolic conservation laws*, SIAM Journal on Numerical Analysis, 59 (2021), pp. 1299–1324.
- [25] Y. LU, S. WONG, M. ZHANG, C.-W. SHU, AND W. CHEN, *Explicit construction of entropy solutions for the Lighthill–Whitham–Richards traffic flow model with a piecewise quadratic flow–density relationship*, Transportation Research Part B: Methodological, 42 (2008), pp. 355–372.
- [26] X. MENG, C.-W. SHU, AND B. WU, *Optimal error estimates for discontinuous Galerkin methods based on upwind-biased fluxes for linear hyperbolic equations*, Mathematics of Computation, 85 (2016), pp. 1225–1261.
- [27] J. QIU AND C.-W. SHU, *Runge–Kutta discontinuous Galerkin method using WENO limiters*, SIAM Journal on Scientific Computing, 26 (2005), pp. 907–929.
- [28] W. H. REED AND T. HILL, *Triangular mesh methods for the neutron transport equation*, tech. report, Los Alamos Scientific Lab., N. Mex.(USA), 1973.
- [29] C.-W. SHU, *Discontinuous Galerkin methods: general approach and stability*, Numerical solutions of partial differential equations, 201 (2009).
- [30] Z. SUN AND C.-W. SHU, *Stability of the fourth order Runge–Kutta method for time-dependent partial differential equations*, Annals of Mathematical Sciences and Applications, 2 (2017), pp. 255–284.
- [31] Z. SUN AND C.-W. SHU, *Strong stability of explicit Runge–Kutta time discretizations*, SIAM Journal on Numerical Analysis, 57 (2019), pp. 1158–1182.
- [32] Z. SUN, Y. WEI, AND K. WU, *On energy laws and stability of Runge–Kutta methods for linear seminegative problems*, SIAM Journal on Numerical Analysis, 60 (2022), pp. 2448–2481.
- [33] Z. SUN AND Y. XING, *On generalized Gauss–Radau projections and optimal error estimates of upwind-biased DG methods for the linear advection equation on special simplex meshes*, Journal of Scientific Computing, 95 (2023), p. 40.
- [34] Q. TAO, Y. LIU, Y. JIANG, AND J. LU, *An oscillation free local discontinuous Galerkin method for nonlinear degenerate parabolic equations*, Numerical Methods for Partial Differential Equations, 39 (2023), pp. 3145–3169.
- [35] Y. XU, X. MENG, C.-W. SHU, AND Q. ZHANG, *Superconvergence analysis of the Runge–Kutta discontinuous Galerkin methods for a linear hyperbolic equation*, Journal of Scientific Computing, 84 (2020), pp. 1–40.
- [36] Y. XU, C.-W. SHU, AND Q. ZHANG, *Error estimate of the fourth-order Runge–Kutta discontinuous Galerkin methods for linear hyperbolic equations*, SIAM Journal on Numerical Analysis, 58 (2020), pp. 2885–2914.
- [37] Y. XU, Q. ZHANG, C.-W. SHU, AND H. WANG, *The L^2 -norm stability analysis of Runge–Kutta discontinuous Galerkin methods for linear hyperbolic equations*, SIAM Journal on Numerical Analysis, 57 (2019), pp. 1574–1601.
- [38] J. YU AND J. S. HESTHAVEN, *A study of several artificial viscosity models within the discontinuous Galerkin framework*, Communications in Computational Physics, 27 (2020), pp. 1309–1343.
- [39] Q. ZHANG AND C.-W. SHU, *Error estimates to smooth solutions of Runge–Kutta discontinuous Galerkin method for symmetrizable systems of conservation laws*, SIAM Journal on Numerical Analysis, 44 (2006), pp. 1703–1720.
- [40] X. ZHANG AND C.-W. SHU, *On positivity-preserving high order discontinuous Galerkin schemes for compressible Euler equations on rectangular meshes*, Journal of Computational Physics, 229 (2010), pp. 8918–8934.
- [41] X. ZHONG AND C.-W. SHU, *A simple weighted essentially nonoscillatory limiter for Runge–Kutta discontinuous Galerkin methods*, Journal of Computational Physics, 232 (2013), pp. 397–415.
- [42] J. ZHU AND C.-W. SHU, *Numerical study on the convergence to steady state solutions of a new class of high order WENO schemes*, Journal of Computational Physics, 349 (2017), pp. 80–96.
- [43] V. ZINGAN, J.-L. GUERMOND, J. MOREL, AND B. POPOV, *Implementation of the entropy viscosity method with the discontinuous Galerkin method*, Computer Methods in Applied Mechanics and Engineering, 253 (2013), pp. 479–490.